STYX Experiment: Gas Mixture, Simulation and Calibration

Alexander Craig Johnston

Masterarbeit in Physik
angefertigt am Physikalischen Institut

vorgelegt der
Mathematisch-Naturwissenschaftlichen Fakultät
der
Rheinischen Friedrich-Wilhelms-Universität
Bonn

Februar 2019

I hereby declare that this thesis was formulated by myself and that no sources or tools other than those cited were used.

Bonn, ...
Date Signature

1. Gutachter: Prof. Dr. Ian Brock
2. Gutachter: Priv.-Doz. Dr. Philip Bechtle

To everyone eager to learn and everyone eager to teach.

Acknowledgements

For inspiring discussions and hardware help such as the (un)screwing of pressure-reducing valves I would like to thank: Ian Brock, Regina Moles-Valls, Ozan Arslan, Oliver Freyermuth, Jochen Kaminski, Irina Cioară, Oliver Ricken, Lara Schildgen, Rui Zhang, Mark Weißenberg, Steffen Schaepe, Jan Stillings, Markus Köhli, Anjishnu Bandyopadhyay, Christian Kirfel, Tanja Holm, Federico Diaz Capriles, Chris Boever, Lucian Scharenberg, Markus Gruber, Michael Kamenar, Maxx Richard Rahman, Barbara Valeriani-Kaminski, Martin Fechtner, Walter Honerbach, Hubert Blank, Andrea Fürstenberg, Nicole Felde, Andreas Valder and Thomas Becker.

Contents

1 Introduction **1**

2 Underlying Physical Principles **3**
2.1 Cosmic Radiation . . . 3
2.1.1 Acceleration Mechanisms . . . 3
2.1.2 Primary Cosmic Ray Composition . . . 4
2.1.3 Secondary Cosmic Rays . . . 4
2.2 Gaseous Ionisation Detectors . . . 6
2.3 Scintillators and Photomultipliers . . . 8

3 Experimental Setup **9**
3.1 Straw Tube Modules . . . 9
3.2 Trigger System . . . 9
3.3 Readout System . . . 10
3.4 Software . . . 11
3.4.1 StyxM2C2 . . . 11
3.4.2 Calibration . . . 11
3.4.3 Reconstruction and Analysis . . . 13
3.4.4 Monte Carlo and Event Display . . . 14
3.5 Typical Experimental Results . . . 15

4 Alignment of the Middle Module **17**
4.1 Method . . . 17
4.2 Results . . . 19

5 Test of Different Gas Mixtures **25**
5.1 Procedure . . . 25
5.2 Straw Mask . . . 26
5.3 Drift Time Spectra . . . 29
5.4 Space-Drift-Time Relation . . . 29
5.5 Efficiency . . . 33
5.6 Recommendation for Gas Mixture and Voltage . . . 38

6 Monte Carlo Simulation **39**

7 Calibration Studies **43**
7.1 Number of Events Used for Calibration . . . 43
7.2 Conclusions and Recommendations . . . 46

8 Summary and Conclusions 47

Bibliography 49

A Fit Results for the Drift-Time-Space Relation 51

List of Figures 53

List of Tables 55

CHAPTER 1

Introduction

Performing an experiment is an art. Physicists try to understand nature and to this end, experiments are indispensable. No theory can be distinguished from speculation unless it yields experimentally testable predictions. Prospective physicists should learn experimenting in order to understand the process of attainment of scientific knowledge. Often, modern experiments are so elaborate an effort, that they are difficult to understand. However understanding an experiment is essential for both the performing experimentalists and those involved in other collaborations of the same field, but also for theorists who interpret the experimental results. The art of experimenting therefore has to be learned and thus taught. There can be no learning without teaching.

The Advanced Laboratory Course [1] is part of the curriculum of the Master's degree programme in both physics and astrophysics at the University of Bonn [2]. The aim of this course is to train students in performing experiments and writing reports on them. One of the experiments offered is STYX (acronym for Straw Tube Young student eXperiment) [3].

STYX is a particle detector detecting ionising cosmic radiation [4]. It consists of modules of the Straw Tube Tracker (STT) [5] from the decommissioned detector ZEUS which was located at DESY, Hamburg, supplemented with scintillators, photomultipliers and electronics. Performing the experiment, students can learn about some characteristics of gaseous detectors and the related electronics. Moreover, knowledge about data analysis using ROOT software and about cosmic rays is thus imparted.

The aim of this thesis is to better understand and to improve the detector performance. Some of the studies carried out to this end are to investigate the alignment of the middle module of STYX with respect to the other two (Chapter 4), the efficiency of its cosmic ray detection and the behaviour of the experiment as various voltages are applied to the modules and various gas mixtures are tested (Chapter 5). The space-drift-time-relation with different gas mixtures is also investigated performing a simulation (Chapter 6). Additionally, the calibration of STYX is studied (Chapter 7). In Chapter 8, the results of the thesis are summarised. Before presenting the studies in Chapters 4-8, the physical principles behind the experiment are explained in Chapter 2, and the experimental setup is introduced in Chapter 3.

CHAPTER 2

Underlying Physical Principles

STYX being an experiment designed for the detection of cosmic radiation, Section 2.1 gives an overview over the phenomenon studied by it. Section 2.2 gives a general introduction to gaseous ionisation detectors, which constitute the main part of STYX. Scintillators and photomultipliers play an important role in STYX as well, therefore they are explained in Section 2.3. The explanations in Sections 2.2 and 2.3 are intentionally generic because the specific usage of those components in STYX is explained in Chapter 3, especially Sections 3.1 and 3.2.

2.1 Cosmic Radiation

Radiation of extraterrestrial origin is called cosmic radiation. A distinction is drawn between primary and secondary cosmic rays. The former are those which originate from a cosmic source, whereas the latter are the products of the interaction of primary cosmic rays with the atmosphere of the Earth.

2.1.1 Acceleration Mechanisms

Although not necessarily all mechanisms by which particles are accelerated to the energies at which they reach Earth are known, there are various physical phenomena yielding high-energetic particles. The following list gives an overview over those acceleration mechanisms that are regarded as especially important [6]:

- **Cyclotron mechanism:** the sun and other stars have magnetic fields created by the turbulent motion of plasma. The areas of the highest field strength are visible as sunspots or star spots. Their creation and decay, i.e. the temporal change of the magnetic fields, induce electric fields that accelerate charged particles. However, in the cyclotron mechanism the particle circulates perpendicular to the magnetic field, and it is unknown by which force it is forced to do so. This shortcoming of the mechanism can be solved with the model of acceleration through sunspot pairs.

- **Sunspot pairs:** two merging sunspots can provide an acceleration mechanism requiring no guiding force. If a sunspot, i.e. a dipole field $\vec{B}$, approaches another with a velocity $\vec{v}$, an electric field parallel to $\vec{v} \times \vec{B}$ is created.

- **Shock acceleration:** supernovae are high-energetic events that release parts of their energy in shock fronts. Those are parts of the material of the dying star that evaporate fast from it. Particles that collide with shock fronts can be reflected and gain energy from the collision, which means they

are accelerated. The acceleration of particles is especially effective if they are reflected multiple times by an inner and an outer shock front.

- **Fermi mechanism:** particles can gain kinetic energy from the collision with magnetic clouds. This mechanism requires a minimal injection energy of the particle because particles lose some of their kinetic energy by interacting with parts of the cloud. Moreover, it requires a minimal lifetime of the cloud because it accelerates particles rather slowly.

- **Pulsars:** pulsars are neutron stars with a strong magnetic field that rotate very fast. From the relation $\vec{E} = \vec{v} \times \vec{B}$ with $\vec{v} \perp \vec{B}$ the fast rotation combined with the strong magnetic field yields a strong electric field $\vec{E}$, which provides a strong acceleration for charged particles.

- **Accretion phenomena:** binary stars, especially those with one compact object (neutron star or black hole) can accelerate particles. The same holds for active galactic nuclei (AGNs), which consist of a supermassive black hole accreting matter. In the latter case, so-called "jets" consisting of accelerated material have been observed. Despite their different size and composition, the acceleration mechanism is similar for binary stars and AGNs. Particles close to the compact object gain high velocities due to the gravitational force. The magnetic field of the compact object can therefore lead to an extrusion of high-energetic particles.

2.1.2 Primary Cosmic Ray Composition

With a fraction of $\approx 85\,\%$, protons are the predominant component of charged primary cosmic radiation [6–8]. The rest is dominated by helium nuclei, followed by nuclei of heavier elements. In general, the abundance of such nuclei falls steeply with the atomic number of the element because of their abundance in the universe, and because they can be fragmented at high energies, but also because lighter elements are easier to accelerate. The flux of different nuclei is plotted against the energy-per-nucleus in Figure 2.1. It shows that the flux decreases as the atomic number increases. Moreover, the flux drops steeply with the energy, except for hydrogen and helium at energies below ≈ 1 GeV per nucleus.

2.1.3 Secondary Cosmic Rays

The atmosphere of the Earth is opaque to cosmic rays, which means that only a small fraction of the protons and a negligible fraction of heavier nuclei reach the ground. The rest interacts with the atmosphere and thus produces secondary cosmic rays. This is the majority of all cosmic radiation that is observed at sea level. The interaction of cosmic rays with the atmosphere can happen through a hadronic or an electromagnetic cascade (also called shower). In a hadronic cascade, kaons and pions are produced in a ratio of $\approx$ 1:9. Kaons predominantly decay into pions, muons, and electrons. The neutral kaon is a superposition of a long-lived state K_L^0 and a short-lived one K_S^0. With a mean lifetime of 9.0×10^{-11} s,[1] the K_S^0 is not able to travel a large distance before its decay if its energy is of the order of some GeV, unlike the K_L^0 with a mean lifetime of 5.1×10^{-8} s. However, this lifetime is not sufficient either for reaching the surface of the Earth in large numbers. The same holds for charged kaons with a mean lifetime of 1.2×10^{-8} s. Neutral pions decay with a lifetime of 8.5×10^{-23} s (practically instantly) into two photons. Charged pions mainly decay into muons and the respective (anti-)neutrino. The lifetime of 2.6×10^{-8} s allows high-energetic charged pions for travelling distances of the same order as long-lived

[1] All particle lifetimes have been taken from [8] without any uncertainties and rounded to two significant digits. This is because the orders of magnitude are most relevant for the considerations presented here, whereas the precise values are not as important.

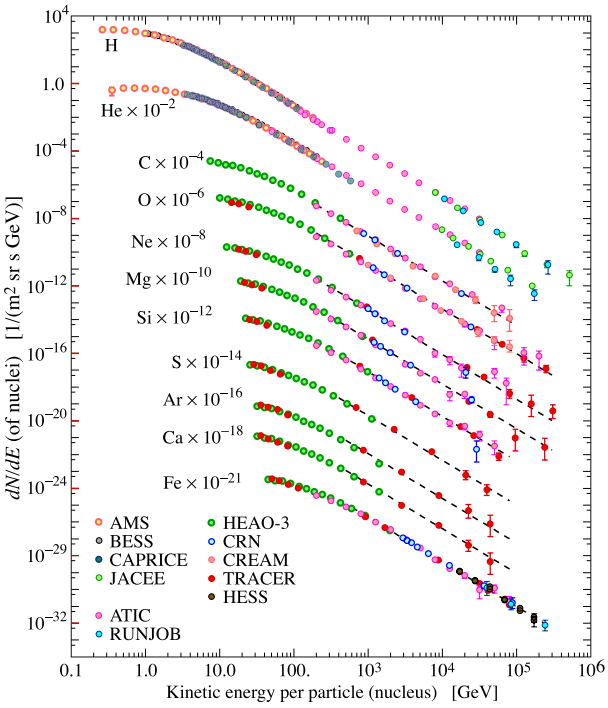

Figure 2.1: Kinetic energy spectrum and composition of primary cosmic rays. Fluxes of different nuclei are plotted in particles per energy-per-nucleus versus energy-per-nucleus. Both axes are logarithmic. The data stems from several different experiments as expressed in the legend. The fluxes are plotted multiplied by different factors for better visibility. Figure taken from [7].

neutral or charged kaons, however the main component of cosmic rays at sea-level consists of muons. Muons are heavier copies of electrons that decay into an electron, a muon neutrino and an electron anti-neutino. Their lifetime of 2.2×10^{-6} s (the longest of all non-stable elementary particles) causes them to travel large distances before their decay. Moreover, their interaction cross-section with matter is lower than for hadrons and electrons, which makes muons more penetrative.

The high-energetic interactions of cosmic rays, especially the decay of the neutral pion, creates high-energetic photons and electrons which can cause electromagnetic showers. In those, photons create electron-positron-pairs in the electric field of atoms, whereas electrons and positrons create photons due to bremsstrahlung when interacting with atoms. This leads to a cascade, until the energy of the created photons does not suffice for pair-creation anymore.

In Figure 2.2, the fluxes of several particle types in cosmic radiation can be seen as a function of the altitude, or equivalently, the atmospheric depth. At sea level, the dominant particles are muon neutrinos and their anti-particles, closely followed by (anti-)muons. Protons and neutrons are rarer by approximately two orders of magnitude. Since the interaction of neutrinos with matter has a very low cross-section, it can only be observed with considerable event rates using very large detector volumes. To an experiment like STYX, they are practically invisible. Therefore, most of the particles detected by STYX are muons.

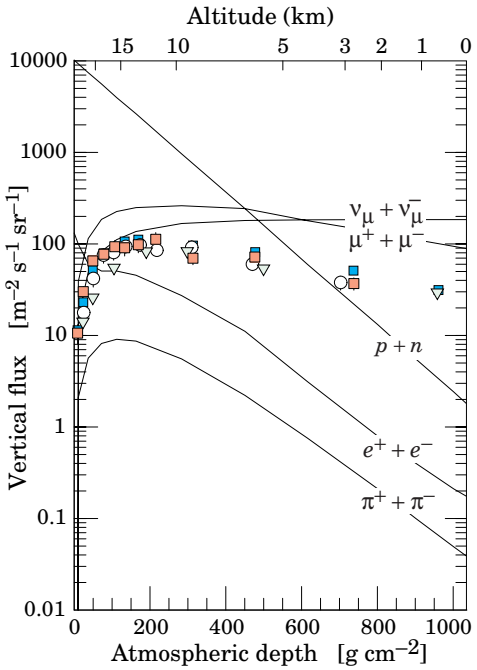

Figure 2.2: Flux of several types of particles in cosmic radiation depending on the atmospheric depth (the mass of air above per unit area). This quantity can also be expressed as the altitude. The particles considered here are muon (anti-)neutrinos, muons, protons and neutrons, electrons and positrons as well as charged pions. Figure taken from [8].

2.2 Gaseous Ionisation Detectors

When charged particles traverse gas, they ionise the medium. Collecting the ions and electrons is, in principle, all that is needed for a gaseous ionisation detector. In order to collect the charge, an electric field is needed. To this end, a voltage is applied to electrodes, such that the electrons and ions are accelerated towards those. The electrode collecting negative charge carriers is called anode, the one collecting positive charges is the cathode. The resulting current needs to be measured to register the ionisation. In almost all realistic cases, the current first needs to be amplified electronically, however. A possible choice is whether one wants to collect only the primary ions and electrons, i.e. those that are produced in the interaction of the charged particle that is detected using the gas, or whether one wants to allow for secondary ionisation and thus an amplification of the signal in the gas. Secondary ionisation is the ionisation that is caused by the primary electrons or ions when they are accelerated so fast that they ionise gas molecules in collisions. This leads to a so-called gas amplification, since the resulting number of ions and electrons is higher than from the primary ionisation.

There are several types of gaseous ionisation detectors, classified according to the type of gas amplification [9]. This depends on the voltage at which the detector is operated and the gas mixture filling it. Depending on the operation mode, a quenching gas is optional or necessary. This is a gas that absorbs photons and dissipates their energy in elastic collisions. Using a quenching gas allows for applying a higher voltage without triggering a continuous discharge in the detector. Therefore, a higher gas amplification can be achieved when a quenching gas is used [9]. Moreover, noise is suppressed by the quenching gas. Due to the absorption of photons and the resulting prevention of additional avalanches, the dead time of the detector, i.e. the time during which it cannot detect additional incident particles

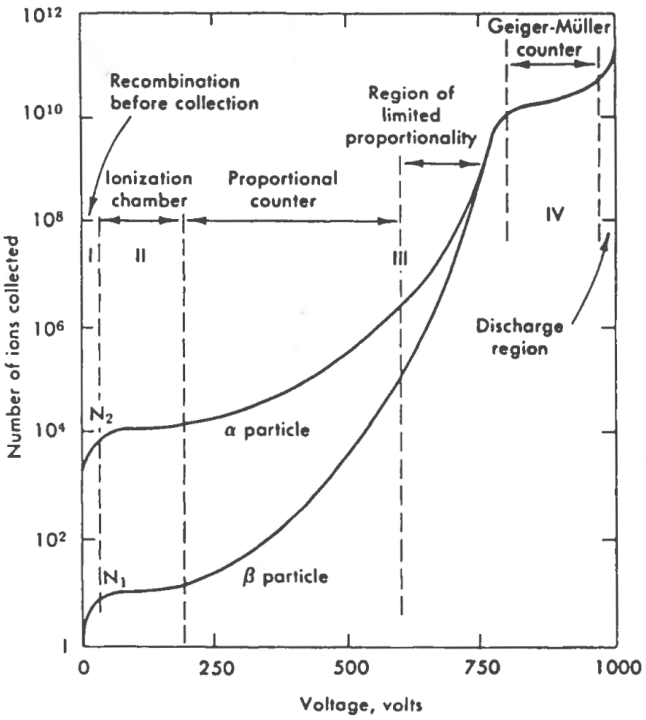

Figure 2.3: Operation Modes of gaseous detectors at different voltages. Source: [10] as cited in [9].

because there are too many ions or electrons near the electrodes, is reduced by using a quenching gas [9].

The various operation modes of a gaseous detector as a function of the voltage are summarised in Figure 2.3.

If the applied voltage is very low, electrons and ions recombine before reaching the electrodes. Therefore, no signal can be measured. This is not an operational radiation detector.

Above a certain voltage, the primary ions are collected, but they cause no secondary ionisation. This setup is called **ionisation chamber**.

At higher voltages, the electrons from the primary ionisation gain an energy sufficient to ionise the gas. Thus, a cascade or avalanche of ionisation follows. The number of collected ions is proportional to the number of primary ions, however. This type of detector operation is called **proportional counter**.

If the voltage is increased further, the proportionality breaks down because the space charge created by the secondary ionisation distorts the electric field. This voltage region is called the **region of limited proportionality**.

A further increase of the voltage leads to an operation as a **Geiger-Müller** or **breakdown counter**. In this case, there is a chain reaction of avlanches over the full length of the anode. Therefore the current is the same for every primary ionisation, regardless of the number of primary ions. In order to stop the ionisation, a quenching gas must be present.

Increasing the voltage beyond the Geiger-Müller region gives rise to a continuous or breakdown discharge. Since this can happen with or without incident radiation, it is not a functional radiation detector. Moreover, this type of operation can cause damage to the detector.

A cylindrical geometry is regarded as simple and advantageous for the amplification of signals. If a Voltage V_0 is applied between an inner cylinder of radius a and an outer cylinder of radius b, the resulting

electric field E at a distance r to the symmetry axis of the setup is given by

$$E(r) = \frac{V_0}{\ln(b/a)r}. \tag{2.1}$$

This means that the mere geometry yields high field strengths for low r, which can only be achieved for a narrow inner cylinder, i.e. a wire. Therefore, many gas detectors feature tubes surrounding a wire with gas in the volume between, and so does STYX.

Another advantage of the cylindrical design is the low capacitance C, which is given by

$$C = \frac{2\pi\varepsilon_0\varepsilon_r}{\ln\left(\frac{b}{a}\right)}L \tag{2.2}$$

for a straw of the length L. Here, ε_0 is the permittivity of the vacuum and ε_r is the relative permittivity of the gas. The low capacitance yields low noise. Moreover, only one readout channel is needed per straw and the volume covered by a straw is relatively large.

2.3 Scintillators and Photomultipliers

A scintillator is a device that emits visible or ultraviolet light when radiation penetrates it. In principle, it can be used as a detector by observing it, but this is normally not viable in particle physics experiments. Instead of the human eye, it is more convenient to use a photomultiplier tube (PMT) [9, 11, 12].

Photomultiplier tubes convert photons into an electric signal. An incident photon can excite an electron from the photocathode by the photoelectric effect. The electron is then accelerated towards a dynode and causes more electrons to be released there. These are then accelerated to the next dynode, s.t. the signal is amplified in each step. Thus, a single photon can cause an observable electric signal [9].

Due to the fast response of scintillators and photomultipliers, they are suitable for usage as a trigger system. Also in STYX, this is their function.

CHAPTER 3

Experimental Setup

In this chapter, the components of STYX are introduced and explained. The straw tube modules (Section 3.1) and the trigger system (Section 3.2) are the components of the experiment that directly interact with cosmic radiation in order to detect it. The readout system is the electronics that is necessary to convert the signals from the modules and trigger to signals suitable for the storage on a computer 3.3. The software used for data processing, reconstruction, analysis and other purposes related with STYX is presented in Section 3.4. The chapter concludes with the presentation of some results that are typically achieved by the students in a usual lab course performance of the experiment (Section 3.5).

3.1 Straw Tube Modules

STYX uses modules from the straw tube tracker (STT) of the decommissioned ZEUS detector. They consist of three layers containing 88 so-called straws. These are tubes with a wire in the centre of their cross-section. The tubes have an inner diameter of 7.495 mm and a length ranging from 20 to 102 cm. Since they consist of carbon fibre with a thin aluminium layer, they are conductive. The copper-beryllium wires in the centre of the straws have a diameter of 50 µm. The arrangement of the straws confers the modules a trapezoidal shape. In the standard setup, the straws are filled with a gas consisting of 82 % argon (Ar) and 18 % carbon dioxide (CO_2). These percentages refer to the volume. Incident charged particles lead to an ionisation of the gas. The CO_2 is the quenching gas (as explained in Section 2.2) that is used in STYX. A voltage of 1 850 V is applied between the wires and the exterior of the straws. This voltage allows for secondary ionisation. This means that the straws are operated as proportional counters.

The three modules of STYX are arranged vertically above each other. This geometry allows for a reconstruction of particle tracks penetrating the three modules. The method of track reconstruction will be described in Section 3.4.

If an ionising particle traverses a straw, electrons and ions are accelerated due to the electric field. The signal thus seen in the straw is called *hit*.

3.2 Trigger System

The trigger system of STYX consists of one scintillator with a photomultiplier tube above and one below the straw tube modules. The scintillators are connected to the photomultipliers via waveguides. An "event", i.e. a situation that is recorded (and in which the detection of a cosmic particle can be expected) is triggered by the coincidence of both photomultiplier signals. As a part of the lab course experiment,

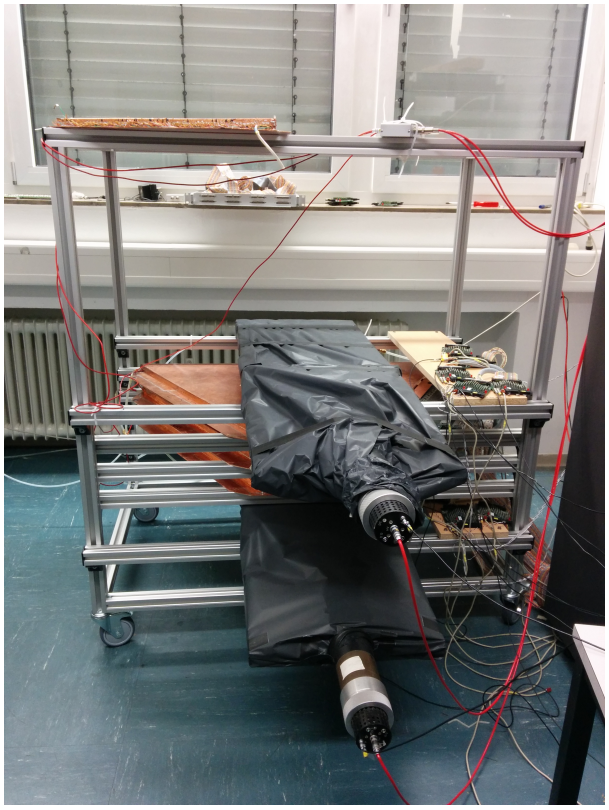

Figure 3.1: The STYX detector. The dark components on top and below are the scintillators and photomultiplier tubes, which are clad in non-transparent plane to shield ambient light. The copper-coloured trapezoidal parts in between are the Straw tube modules. In these, the straws are arranged parallel to the two sides of the trapezium that are parallel to each other. Image taken from [13].

the student groups have to find suitable operating voltages for both photomultipliers. At too low a voltage, the amplification in the PMT might be too low to register events efficiently, whereas at too high a voltage, the amount of noise increases, rather than the number of detected particles.

3.3 Readout System

The signals from the straws are processed by Front-End (FE) boards. These comprise amplifiers, shapers and discriminators in so-called "ASDQ" chips, the name of which refers to the fact that the chip amplifies, shapes, discriminates and measures charge [14]. Each of these chips is for six straws. The output signals from those six straws are time-multiplexed, i.e. given to one single channel with a time offset of 200 ns. Therefore the readout window is 1 200 ns. A module is connected to two large FE boards with 16 channels (i.e. it reads out 96 straws) and a small one with 12 channels (i.e. 72 straws).

The necessary supply voltage for the FE boards and the ASDQ chips is provided by driver boards. These stabilise and filter the original supplied voltage.

The signal from the FE boards is processed by the time-to-digital converter (TDC) readout board (TRB). The TRB has four inputs with 32 channels each, where 31 are used to read the signal from the straws and one for the trigger. The FE boards are connected to the TRB via a converter box that has been built for this purpose. Since this box only has eight slots, one FE board is not connected. This is the one

that would read out the right 72 straws (the right 24 ones of each layer) of the middle module if it was connected [15, 16].

3.4 Software

The raw data collected by the experiment are the signals from individual channels, which contain times with respect to the trigger, at which there is a signal in the straws, plus the respective time delay from the time-multiplexing. In order to analyse the data collected by the experiment, it is converted to an event-by-event file containing the drift times t_{drift} for each straw with a hit in it. To this end, there are several software components that are used for three steps: data processing (also called StyxM2C2, standing for merge, map, calibrate and convert, Section 3.4.1), calibration (Section 3.4.2), as well as reconstruction and analysis (Section 3.4.3). The general scheme in which the steps succeed is the following: StyxM2C2 converts the raw data into a file containing uncalibrated drift time information for each straw. This file is used as the input of the calibration. The output of the calibration is a text file containing information about the status and time delay of each straw as well as a ROOT file which can be used to inspect the calibration process. The text file containing information about each straw is passed to StyxM2C2, together with the raw data, to create a text file containing calibrated drift time information for each straw. This text file is used as the input for the event reconstruction producing a ROOT file with reconstructed events as its output. This Root file can then be analysed to derive information, for instance to create plots. The following three subsections give more detailed information about the individual steps.

Additionally, STYX features software in order to perform a Monte Carlo simulation of the experiment and an event display visualising data or Monte Carlo events (Section 3.4.4). All software can be found in a git repository [17].

3.4.1 StyxM2C2

StyxM2C2 is a programme that processes the raw data and produces a text file with the drift time information for the subsequent analysis steps. The leading and trailing edges of events are merged by the programme, and the channels are demultiplexed, such that the signal is mapped to the single straws. Empty events, i.e. those that contain less than four hits, are discarded. This is because at least five hits are required to reconstruct a track, see Section 3.4.3.

If no calibration file is provided, the drift times in the output file are times that pass between the trigger and the straw signal. They are uncalibrated, i.e. there may be a time delay. This can be different for each straw. If a calibration is applied, the offset is compensated for. Therefore, the drift times in the output of StyxM2C2 are compatible with each other and should correspond to the actual drift time in the straw.

3.4.2 Calibration

Since the processing of the signal takes differently long for different channels, and since there can be a different amount of noise and signal in each straw, a calibration needs to be applied. The calibration subtracts the time offset from the signal by shifting the peak of the drift time distribution towards the reference time. All noise before the signal is thus cleared. Moreover, the calibration assigns a status to each straw depending on whether they can be calibrated or not (and in which way the calibration fails, if it does). A straw that seems to work properly is called “ok” (sometimes also the word “working” is used). If the straw shows no or only very little signal, it is called “dead”. A straw which gives a permanent signal without any strong dependency on the trigger time is called “hot”. If none of the criteria for the mentioned statuses is fulfilled, the straw is assigned the status “continuous”.

The method by which the calibration is done is the following: for each straw a histogram is filled, which contains the number of signals depending on the time. This is a so-called drift time spectrum. For an uncalibrated straw without any significant malfunction, the spectrum shows a peak after a certain time. Before that, there are also entries, which are mostly noise. An example can be seen in the top left histogram of Figure 3.2. In the calibration procedure, a linear function is fitted to the raising edge of the drift time spectrum. The zero of this function is the time offset, which is subtracted from the drift time in that straw. For the calibrated straw, the histogram entries are shifted leftwards (i.e. the time offset is subtracted) and the noise is removed. This can be seen in the top right part of Figure 3.2.

This can also be plotted for all straws of one layer at the same time. In the bottom histograms of Figure 3.2, the x-axis contains the straw number, the y-axis the drift time and the z-axis (colour-code) gives the number of entries. Therefore, each x-axis bin of the bottom histograms of Figure 3.2 contains a plot analogous to the top histograms. One can observe that the time shift can differ for different straws and that some straws are left out after the calibration. This is because the straws are hot, dead or continuous. The straws with numbers 3 and 4 give very many hits before the calibration, which means they are probably hot. Straws 36 and 37 give exceptionally few hits, which means they are probably dead.

Examples for the drift time spectra of malfunctioning straws can be seen in Figure 3.3. Those plots contain the spectrum before calibration. Afterwards, the histograms are empty.

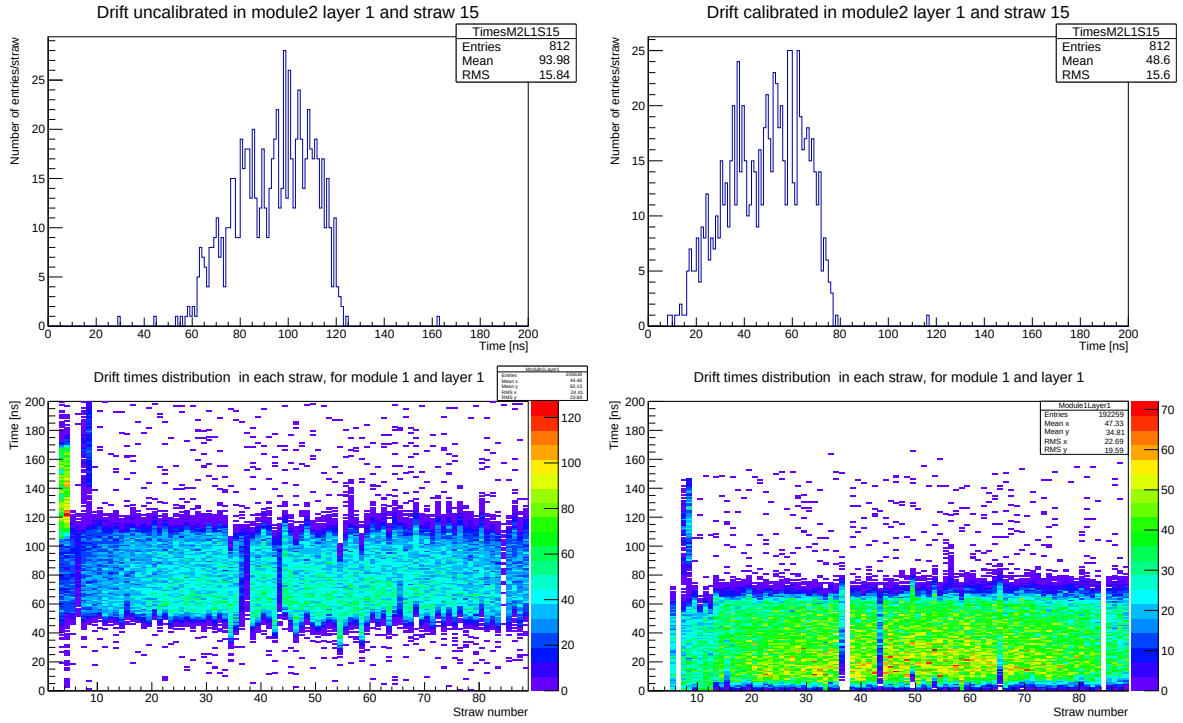

Figure 3.2: Drift time spectrum of one straw before (top left) and after (top right) calibration. This straw is classified as “ok”. The time axis of the left histogram is given by the trigger signal. The histogram is filled with signals from the straw. In the calibration, a time offset is subtracted and noise is cleared. Therefore, the right histogram is shifted leftwards. Ideally, the peak would start at 0 ns. The bottom histograms contain the analogous plot for one straw per bin on the x-axis. The y-axis gives the time information and the z-axis gives the colour-coded number of entries.

In order to avoid biasing the data sample in the calibration, the data set is split into one part to obtain the information that is needed for the calibration, and another one, on which the information is applied. Typically, 300 000 events are used for the calibration of a data sample that is taken overnight and typically

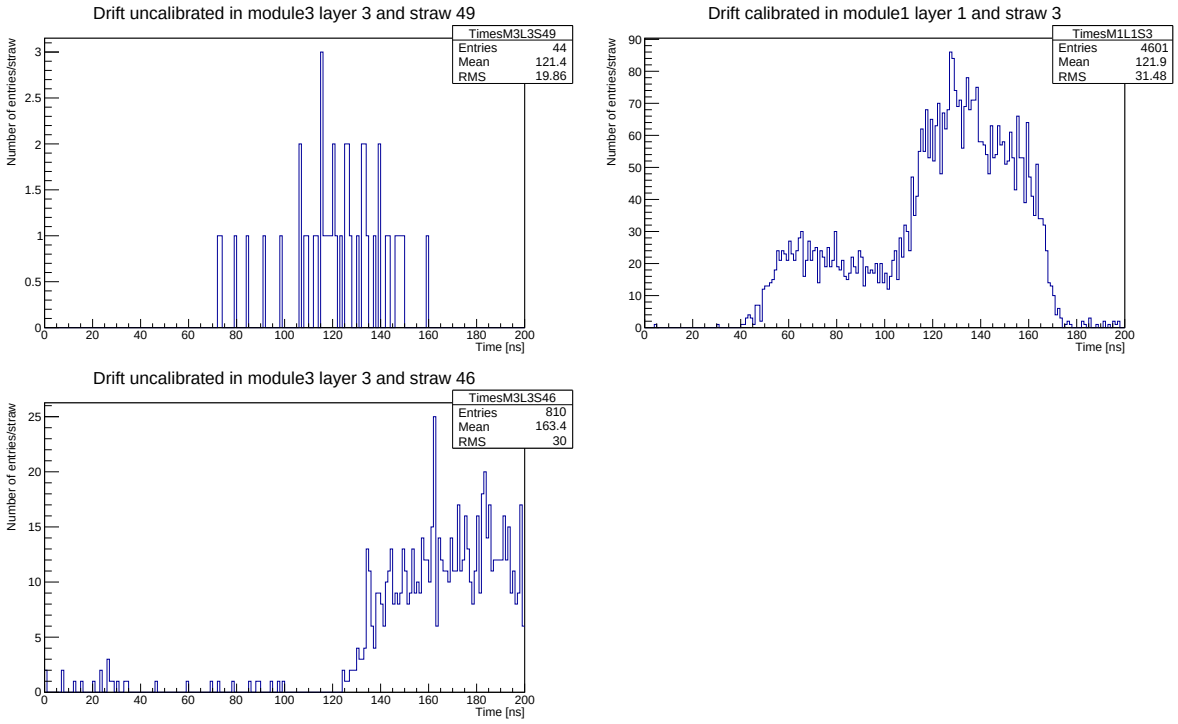

Figure 3.3: Drift time spectra of different malfunctioning straws before calibration. After calibration, the corresponding histograms are empty because they are cleared for all straws that are not marked as ok. On the top left, a dead straw with few entries can be seen. There are also dead straws without a single entry. The top right histogram shows the drift time spectrum of a hot straw. The number of entries is relatively high and the drift times cover a wide range. The bottom histogram presents the drift time spectrum for a continuous straw. In this particular case, a considerable part of the spectrum seems to be outside of the time window. The peak is relatively wide and there is a considerable number of entries over a wide range in time before the peak. The number of entries is not as low as for a dead straw, but rather low compared with an ok straw. The spectrum of such a straw can be seen in Figure 3.2 before and after calibration. It should not be forgotten, that that straw is shorter than the continuous one shown here (which can be seen from the straw number because the counting starts at the shortest straw in a layer). Therefore, a similar number of entries corresponds to a different detection efficiency for both straws.

contains $\gtrsim 1$ million events. In Chapter 7 it will be checked whether the choice to use 300 000 events for the calibration is sensible.

The information on the straw statuses can easily be seen from the so-called straw mask. An example for it can be seen in Figure 3.4. It is a graphical representation of a cross-section through STYX orthogonal to the straws. The straws are plotted in different colours that correspond to their respective status. The unconnected straws of the middle module are marked as dead.

3.4.3 Reconstruction and Analysis

After the calibration, a drift radius can be reconstructed from the drift times. This is done using a built-in space-drift-time relation (also called *t-r* relation). This is a cubic polynomial that converts the drift time t_{drift} into a radius r_{drift}. If a hit is seen in a straw in the middle layer of a module, the neighbouring straws are searched for hits. This is in order to reconstruct *segments*, which is the appellation for tangents to at least two hits.

There are two algorithms in order to construct a segment. One starts with a hit in a straw in the middle

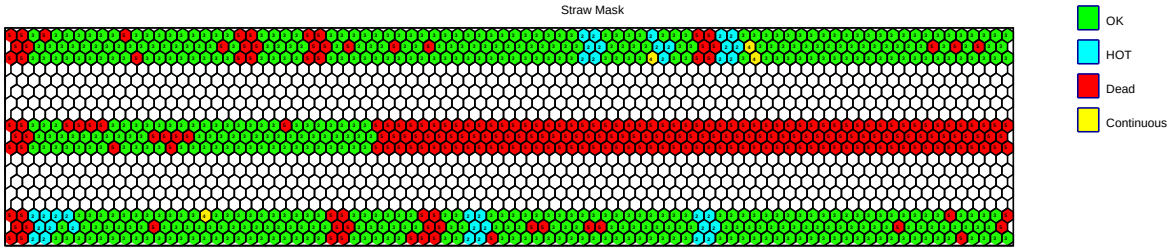

Figure 3.4: An example of a straw mask, obtained from the calibration of STYX. In this case, not only the straws connected to the right FE board are marked as dead, which always is the case, but also those connected to the middle FE board. A possible reason for such an outage of an entire FE board is a defective connection to the driver board supplying its power.

layer (the so-called seed straw) of a module and searches the two straws above and the two below it for further hits (i.e. the straws with number n and $n-1$, where n is the number of the seed straw). If there are some, the algorithm fits all possible segments to the hits. This algorithm is sometimes called the four-neighbouring-straws algorithm.

The second segment-creating algorithm starts with a hit in a straw in the middle layer, too. It searches the neighbouring straws in the middle layer, but also four straws above and below the seed straw (i.e. if the seed straw has the number n, it searches in the straws with numbers $n-2, n-1, n, n+1$ in the top and bottom modules and the straws with number $n \pm 1$ in the middle module). Also with this algorithm, all possible segments are fitted to the hits.

From the segments, a *track* is reconstructed. This is done if a segment candidate from the top and the bottom module have the same direction with in some tolerance margin. If no matching segments are found, the algorithm searches for a fitting combination of a segment and a *cluster*, which is a group of two hits in adjacent straws which does not yield a suitable segment. An event can only contain two segments in different modules if it contains at least six hits. For a segment and a cluster in different modules at least five hits are required. Therefore events with fewer hits are discarded by StyxM2C2. The middle module is not used for track reconstruction.

The assumption, that particle tracks are not curved, although they are inside the magnetic field of the Earth, is justified because at typical particle energies the curvature can be neglected. From the formula $p[\mathrm{GeV}] = 0.3B[\mathrm{T}]r[\mathrm{m}]$ [6], p.81 it can be seen that in the Earth's magnetic field with $B = 48 \times 10^{-6}\,\mathrm{T}$ [18], a radius $r \lesssim 10\,\mathrm{m}$[1] requires that the particle momentum p is $\lesssim 0.144\,\mathrm{MeV}$. At such a low momentum, the muon would travel $\approx 0.6\,\mathrm{m}$ during its mean lifetime. Moreover the energy loss per distance of such a low-energetic muon would be too high for it to penetrate much material. The other way around, from the fact that a particle reaches the experiment (travelling a long way through the atmosphere and the ceiling of the room STYX is in), it can be assumed that the particle is (approximately) at minimum ionisation. For a muon, this corresponds to a momentum between $\sim 100\,\mathrm{MeV}$ and $\sim 10^1$ GeV (see Fig. 33.1 in [8]).

3.4.4 Monte Carlo and Event Display

In order to compare the data with the expectation, there is a simulation of the detector geometry and the signal that has to be expected from particles traversing the modules. It is expected that cosmic particles follow a $\cos^2\vartheta$ distribution. In the simulation, a *r-t* relation is used, which gives a drift time for a known

[1] which is probably an overestimate of the maximal radius that can be distinguished from a straight line on the scale of STYX

radius. This is because the distance between a particle track and a wire is the known quantity in the simulation. The *r*-*t* relation is a cubic polynomial that is an approximate inverse of the *t*-*r* relation. The simulation does not take into account, however, that the detection efficiency of the straws and the scintillators can vary and will always be below unity. This can be caused by straws not fulfilling the calibration criterion or a signal that is too small to be distinguished from noise. The attenuation and energy distribution of particles is not simulated. This can be justified because from the previous considerations, the particles are near minimum ionisation. The fact that particle tracks are simulated as straight lines is as justified as it is for the actual particles.

3.5 Typical Experimental Results

The instructions to perform STYX as part of the lab course is described in [19]. Here, they are summarised in a descriptive manner.

Students performing the STYX experiment as part of the lab course typically start with setting the voltage of the photomultipliers in order to find the best trigger settings. They start with one photomultiplier and denote the count rate for different voltage. An exponential increase, followed by a slower, linear one can be seen and the best operation point is found at the transition of both. This is because the linear increase only accumulates noise, whereas the exponential is due to the intrinsic amplification. Afterwards, the voltage of the other PMT is varied while the first one is kept constant. A linear increase, followed by a plateau is seen and the lower margin of the plateau is set as the operating voltage.

After the determination of the PMT voltages, the students perform short data takings with different threshold voltages of the Front-End-Boards. This is also called threshold scan. They see how the amount of noise decreases, but also the amount of signal, if the threshold voltage is set too high. They then decide for a value of the threshold voltage, with which they start an overnight data taking.

On the following morning, the experiment has typically collected $\gtrsim 10^6$ events. With the first 300000 of those, the students perform the calibration. From the hence produced straw mask, as seen in Figure 3.4, they can see which straws are working and which ones do not. In the discussion of the calibration with the tutor, plots like Figures 3.2 and 3.3 are typically scrutinised.

The calibration obtained is applied to the remaining data. The events which have been used for the calibration are discarded in order to avoid a bias. The result is a calibrated data file which is analysed using the reconstruction and analysis software.

Analysing the reconstructed data offers the students the opportunity to compare the angular distribution of tracks and segments as reconstructed with the two different algorithms. For example, the angle of the segments and the angle of the tracks can be filled into a two-dimensional histogram for both algorithms separately or at the same time. Further cuts may be applied, e.g. only events with one track. The resulting plots can be seen in Figure 3.5. Moreover, the angular distribution of particles can be observed and compared with the $\cos^2 \vartheta$ law one expects. A typical resulting plot is Figure 3.6. The analysis procedure allows the students to become more familiar with the analysis software ROOT. For many, it is their first encounter with this software.

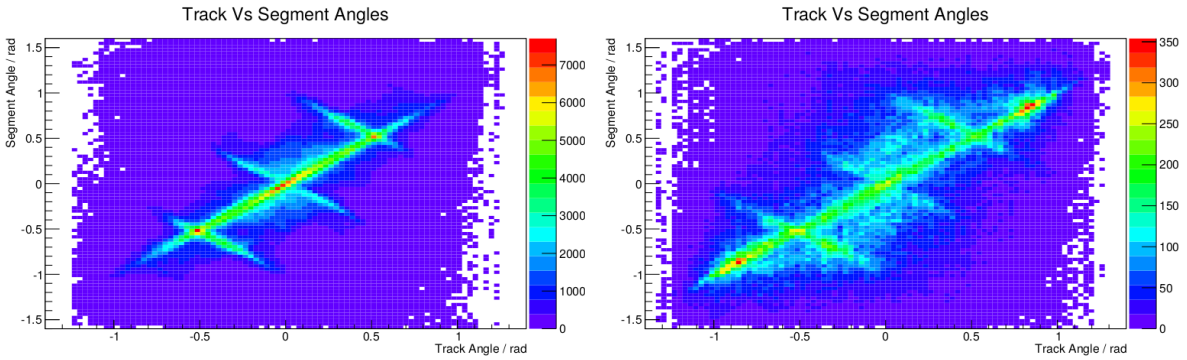

Figure 3.5: Histograms for the distribution of track and segment angles for events with one track as produced in the lab course. The left plot shows the distribution for events where the track was reconstructed using the segment matching algorithm, the right plot for the one that matches segments and clusters.

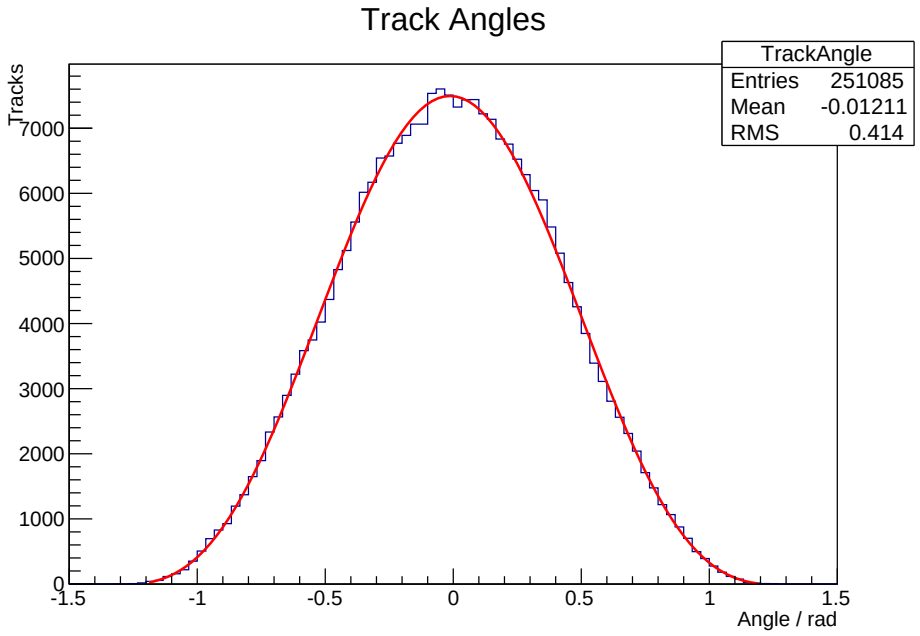

Figure 3.6: Histogram of the track angles with a cosinusoidal fit function.

CHAPTER 4

Alignment of the Middle Module

The mounting of the modules of STYX does not guarantee an alignment more accurate than $\sim 1\,\mathrm{mm}$. Further accuracy has to be achieved through data analysis. A well-aligned detector is important because any offset produces distortions of the data, that might be misinterpreted as physical effects.

4.1 Method

Mounting the middle module with higher precision than before is neither promising nor necessary. Instead, the offset is determined from the data and included in the reconstruction and analysis software, such that it is being compensated.

The underlying idea is to look at the difference between a track position that is reconstructed using the segments (or segment and cluster) in the top and bottom module and the measured track position in the middle module. However, a problem is inevitable here: the straws only provide a radius r with respect to the central wire, but not a sign, i.e. whether a particle passed left or right of the wire.

Therefore, the distance of a track from the centre of a straw d_{track} is defined as a signed quantity

$$d_{\mathrm{track}} = \frac{z_{\mathrm{straw}} \times s - x_{\mathrm{straw}} + x_{\mathrm{offset}}}{\sqrt{1 + s^2}} \tag{4.1}$$

making use of the coordinates z_{straw} and x_{straw} referring to the position of the centre of a straw and the observable s is the slope of the track. The horizontal axis orthogonal to the straws is x, the vertical axis z. The coordinate parallel to the straws is y, but it is not used, as the experiment cannot collect any information on it. The origin of the z-axis is identical with the height of the centres of the straws in the middle layer of the bottom module. The origin of the x-axis is two times the straw width left of the centre of the shortest straw in the middle layer of the bottom module, if the straws get longer to the right. The slope s is defined as $\frac{\Delta x}{\Delta z}$. If it was defined as $\frac{\Delta z}{\Delta x}$, it would be infinite for vertical particle tracks, which occur very often. Horizontal tracks are unproblematic because they are relatively rare and they cannot cross both scintillators. This means such a particle can only be detected if the event is triggered by another one that penetrates the detector at the same time, which is also quite rare. Note that $z_{\mathrm{straw}} \times s$ corresponds to the x-value of the track at the height z of the straw. The crucial quantity for determining the alignment is the offset in horizontal direction x_{offset}.

In order to measure x_{offset}, the following strategy is used: a certain value of x_{offset} is assumed and the absolute value of the track distance $|d_{\mathrm{track}}|$ is compared with the drift radius r_{drift}. The thus obtained residual $R = |d_{\mathrm{track}}| - r_{\mathrm{drift}}$ approaches zero for a well-aligned detector if there are no additional errors.

It can, however, also be zero if both quantities have the same absolute value, but the track is being reconstructed on the wrong side. Therefore, positive and negative distances are treated separately and one defines a positive residual $R_+ = (|d_{\text{track}}| - r_{\text{drift}}), \forall d_{\text{track}} \geq 0$ and a negative residual $R_- = -(|d_{\text{track}}| - r_{\text{drift}}), \forall d_{\text{track}} < 0$. The first sign guarantees a consistent behaviour of R_+ and R_- in case of an offset in the same direction.

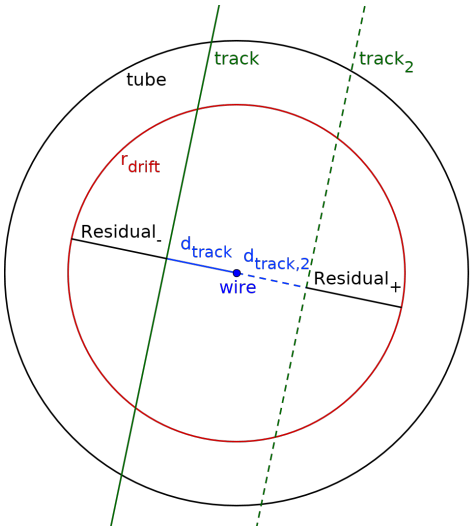

Figure 4.1: Visualisation of different residuals. The sketch shows the cross-section through a straw in the middle module, the central point is the wire and the outer circle is the tube. A track (solid green line), which is as always reconstructed using the top and bottom module has a distance d_{track} to the straw centre (and to the wire, if the wire radius of 25 µm is neglected). The straw observes a drift radius r_{drift} (red circle) and the difference between r_{drift} and d_{track} is the residual. Here, it is called Residual_ ($\equiv R_-$). The straw in the middle module does not give any information on the track direction, which means that the particle can have passed through the straw on any tangent to the circle (neglecting errors on r_{drift}). In particular, it can pass on either side of the wire, assuming that the slope of the reconstructed track does not differ strongly from the one of actual particle slope. If the alignment is very poor, the track may cross the straw on the other side of the wire, which is denoted here by track$_2$ (dashed green line). The residual on the other side is called Residual$_+$ ($\equiv R_+$). The unsigned residual R would have the same value in both cases, whereas here, the distinction between R_- and R_+ can be seen. Figure created using GeoGebra [20].

In the case of an ideal alignment, the distribution of residuals approaches the form of a Gaussian function $f(x) = a \exp\left(\frac{(x-\mu)^2}{2\sigma^2}\right)$ for a sufficiently large number. The parameter a equals the height of the function at its maximum and depends on the number of events used since no normalisation of the function is applied. This is because the height is not considered here. The parameter μ equals the mean of the function. In the case of an ideal alignment, it should be zero. The width of the curve is quantified by the parameter σ. For an ideal alignment, σ corresponds to the intrinsic detector resolution. Since a wrong value of the offset would distort the distribution, the narrowest curve will be obtained for the correct offset. However, the width does not necessarily equal the best resolution that could in principle be achieved with the straws because other effects can broaden the distribution, particularly a rotation of the middle module with respect to the others or a wrong t-r relation.

In order to find the offset where the distributions are the narrowest, x_{offset} is set to values in steps of 0.1 mm and the width of a fitted Gaussian curve is evaluated.

A second method is to consider the mean μ of the Gaussian that is fitted to the distribution of the respective residual. As mentioned before, the mean is zero if the offset that is assumed is correct.

A caveat that needs to be considered is that the shape of the residual is not perfectly Gaussian. In

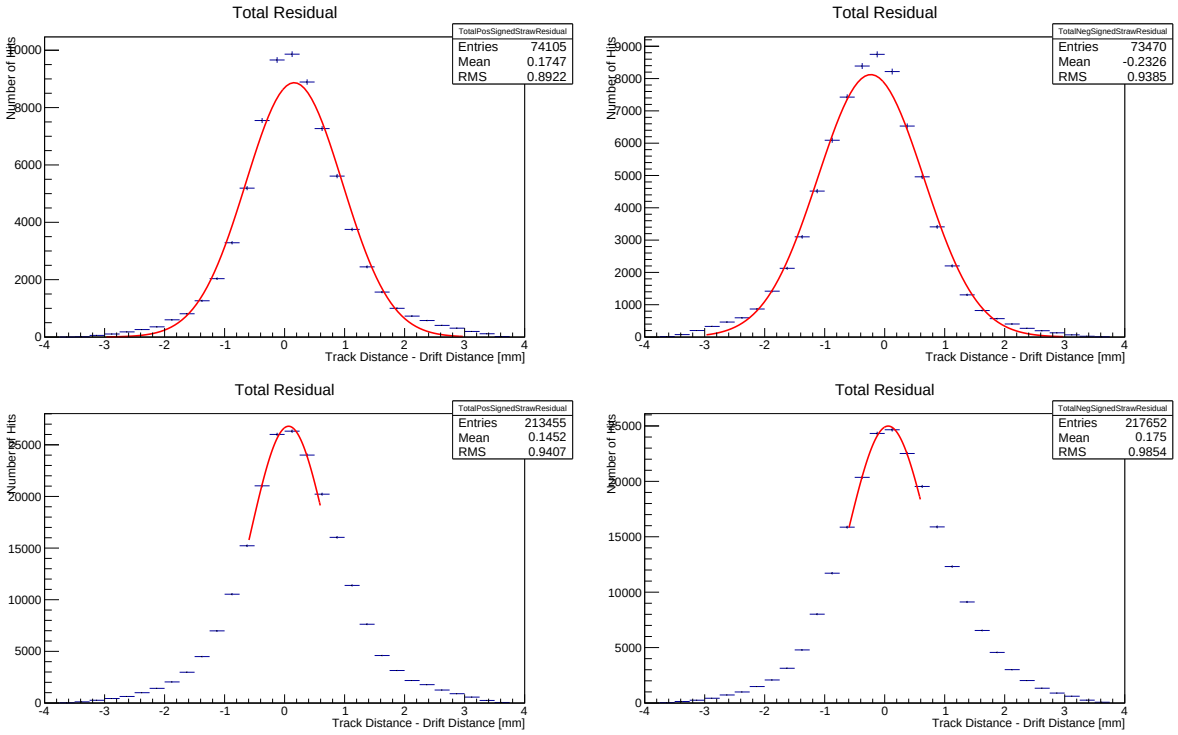

Figure 4.2: Positive (left) and negative (right) residuals R_+ and R_- fitted over a large range (namely -3 mm to 3 mm, top) and over a low range (namely -0.6 mm to 0.6 mm, bottom). On the histograms in the top row, it can easily be seen that the fit is very poor in the centre of the distributions. For the small range as seen in the bottom row, the function fits the distribution better, but this says nothing about the outer parts of the distribution.

fact, it is not even necessarily symmetric. If the fit range is too large, the tails of the distribution have a negative influence on the quality of the fit near the centre. Two examples for quite poor fits where the fit range is large can be found in the top row of Figure 4.2.

Decreasing the fit range yields larger uncertainties on the parameters, but the function fits the data much better near the peak. Here, a range from -0.6 mm to 0.6 mm is chosen. This roughly corresponds to a range from $-\sigma$ to σ. Two example plots of where the small fit range can be seen are in the bottom row of Figure 4.2.

4.2 Results

The narrowest shape of both residuals R_+ and R_- (expressed through the parameter σ of the Gaussian function) is found if the offset is $x_{\text{offset}} = -0.6$ mm.

Table 4.2 shows for R_+ and R_- and the means of both distributions shift in opposite directions when x_{offset} is varied. This is to be expected because both quantities are defined as opposite signed. At the correct offset, the distribution can be expected to be centered around zero. Therefore, the mean μ of the distributions is plotted against the offset and a line is fitted to it. This has been done for both residuals. The plot can be seen in Figure 4.3.

Table 4.1: The positive and negative signed residual R_+ and R_- yield distributions if one assumes and offset x_{offset}. For each offset, a Gaussian function is fitted to the distribution. The standard deviation σ and its uncertainty $\Delta\sigma$ are given for both residuals separately here.

	R_+		R_-	
x_{offset}/mm	$\sigma/10^{-1}$ mm	$\Delta\sigma/10^{-2}$ mm	$\sigma/10^{-1}$ mm	$\Delta\sigma/10^{-2}$ mm
−0.9	7.05	1.9	7.14	1.9
−0.8	6.85	1.7	6.94	1.8
−0.7	6.64	1.5	7.03	1.8
−0.6	6.31	1.3	6.83	1.7
−0.5	6.42	1.4	6.83	1.7
−0.4	6.50	1.4	6.92	1.8
−0.3	6.65	1.5	7.28	2.0
−0.2	6.93	1.7	7.54	2.3
−0.1	7.51	2.3	8.16	3.0
0.0	7.59	2.4	8.21	3.0
0.1	7.39	2.3	8.65	3.6
0.2	7.56	2.5	8.96	4.1
0.3	8.11	3.2	9.03	4.2

Table 4.2: Mean μ of the Gaussian functions fitted to the positve and negative signed residuals R_+ and R_-, together with the respective uncertainty $\Delta\mu$.

	R_+		R_-	
x_{offset}/mm	$\mu/10\,\mu$m	$\Delta\mu/\mu$m	$\mu/10\,\mu$m	$\Delta\mu/\mu$m
−0.9	26.7	15	−10.93	7.7
−0.8	21.9	12	−6.23	6.7
−0.7	16.15	8.8	−2.07	6.1
−0.6	10.45	6.2	2.35	5.8
−0.5	6.67	5.6	5.83	6.3
−0.4	1.38	5.1	8.82	7.2
−0.3	−4.19	5.6	13.08	8.4
−0.2	−9.51	6.8	17.1	12
−0.1	−16.7	12	21.6	17
0.0	−22.5	15	23.5	18
0.1	−26.0	17	25.4	23
0.2	−31.4	21	26.7	26
0.3	−38.9	31	28.6	28

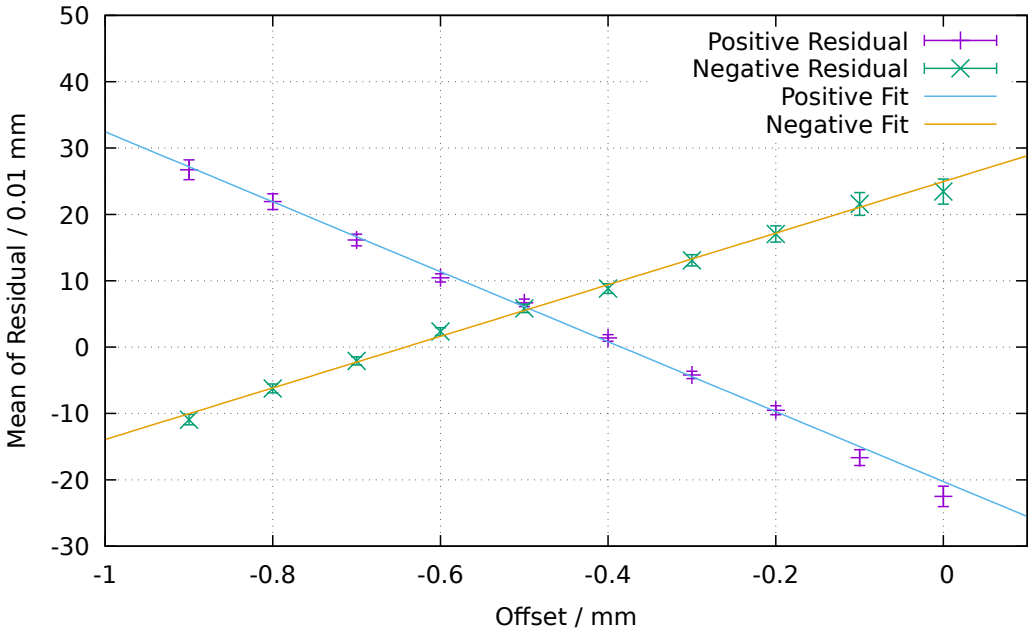

Figure 4.3: The mean μ of the residual is plotted against the assumed offset x_{offset} for the positive and negative signed residual R_+ and R_- separately. To both, a line is fitted.

The resultant fit functions are

$$f_+(x) = (-52.7041 \pm 1.275) \times 10^{-2} x_{\text{offset}} + (-20.2565 \pm 0.6038) \times 10^{-2}\,\text{mm} \tag{4.2}$$

$$f_-(x) = (38.8699 \pm 0.8677) \times 10^{-2} x_{\text{offset}} + (24.9514 \pm 0.5317) \times 10^{-2}\,\text{mm}, \tag{4.3}$$

where f_+ is the fit for the mean of R_+ and f_- for the mean of R_-. Setting both quantities to zero and solving for x_{offset} yields the offsets

$$x^+_{\text{offset}} = (-0.384 \pm 0.015)\,\text{mm} \tag{4.4}$$

$$x^-_{\text{offset}} = (-0.642 \pm 0.020)\,\text{mm}. \tag{4.5}$$

The result x^+_{offset} from the positive residual and the one from the negative residual, x^-_{offset} strongly differ. The discrepancy is an order of magnitude larger than the uncertainties on both quantities. The value of x^-_{offset} seems to be consistent with the offset of -0.6 mm that the method of the narrowest distribution suggests. However, it might be questioned that the accuracy of such a determination is no larger than 0.020 mm. Since the distributions, to which a Gaussian function has been fitted, do not necessarily have a truly Gaussian shape, it is possible that a deviations from the shape introduce a systematic shift to both distributions, perhaps in opposite direction due to the opposite sign in their definition.

If that is the case, it makes sense to consider the intersection of both fit lines, which is at $x_{\text{offset}} = (-0.494 \pm 0.012)$ mm. This is also the value that would approximately result, if one would not use the sign in the definition of the residuals R_+ and R_+ so that one use an overlay of both.

The fact, that the width of the distribution of residuals never falls below ≈ 0.6 mm might however hint at sub-optimal circumstances, because this value is more than the ≈ 200 to $\approx 300\,\mu$m resolution that have been achieved for the ZEUS STT [5] and that may be expected, if STYX is operated under ideal conditions.

This may have different reasons: the three layers of the modules might have a different offset each. This can be investigated by the same procedure as before, by only considering a single layer at one time. However, no difference between the offset yielding the minimal width has been found for the different layers. Moreover, even within a layer the distances between the straws might vary due to flaws of the manufacturing process. Investigating an offset for each straw individually is also possible in principle, however the statistics of an usual data taking will hardly be sufficient. It is not easy to estimate the minimum number of hits that is needed in a straw to determine the residuals without statistical fluctuations ruining the precision. However, 50 000 hits seem to be a sensible number, which would mean 25 000 for R_{-} and R_{+}. Figure 4.4 shows the number of hits in each straw of the middle module for a typical data taking of $\approx$ 16 hours. Out of those, $\approx$ 3 hours are needed for the calibration because experience shows that the event rate is $\approx$ 100 000 h. Increasing the number of hits by a factor 12, which means that most of the straw with numbers $\geq$ 18 would contain enough hits, would therefore require a data taking of approximately $12 \times 13\,\text{h} = 156\,\text{h}$. Accordingly more time would be needed for the straws with lower hit numbers.

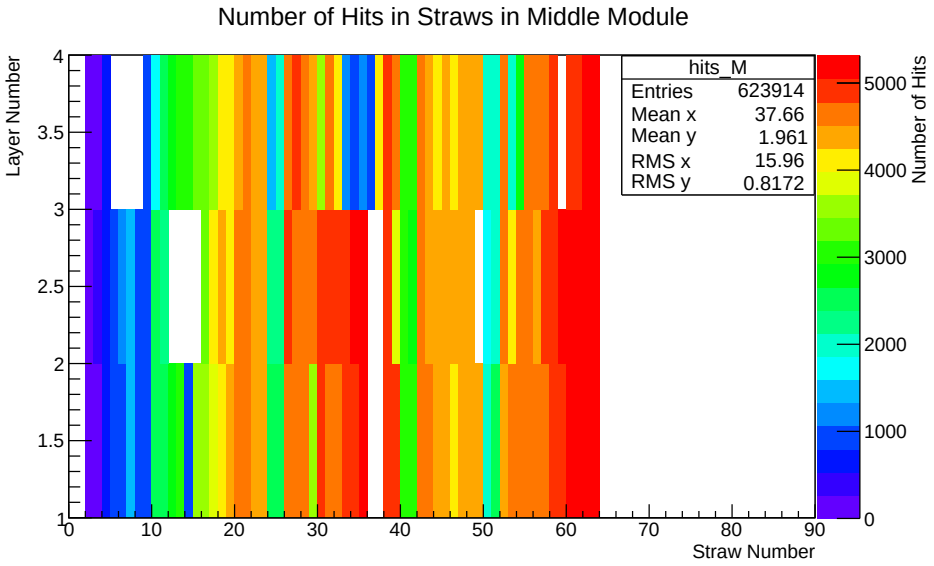

Figure 4.4: Numbers of hits in the straws of the middle module. This plot is produced from a data sample taken over one night ($\approx$ 16 hours). The right straws are empty because the right third of the module is not connected to the read-out system. The number of hits in a straw decreases to the left, because from the perspective of the central straws, the scintillators cover a larger solid angle. This means that a larger number of particles is able to cross these straws *and* to trigger an event.

Another possible reason might be a torsion of the experiment, which means the straws of the middle module are not exactly parallel to the ones of the top and bottom module. This would lead to an offset in different directions at the opposite ends of the straws. Unfortunately, this effect can not be studied because the hardware does not allow for any information of the position of a hit along the straws. In order to investigate this, it is necessary to install additional scintillator stripes perpendicular to the straws, or to investigate it with a radioactive source.

A third reason for the existence of large residuals might be a mismatch between the expected or observed track and the true one. This can be caused by a wrong track reconstruction or a poor calibration of some straws.

A fourth reason for residuals that are too large, is if the drift radius r_{drift}, which is calculated from

the drift time t_{drift}, is wrong. In other words, this would be the case if the relation between drift time and drift radius, the true *t-r* relation is different than the one that is implemented in the STYX code. A comparison between a simulation and the STYX code can be found in Chapter 6. To anticipate the result, Figure 6.3 shows that for a fixed drift time, the radius from the STYX code is almost always smaller than the result derived from the simulation. Especially at intermediate times and radii, the difference can reach about 300 µm to 400 µm. Therefore, a residual will take values different from zero even though the track is reconstructed correctly and the drift time is correct, since r_{drift} is calculated as to be smaller than it actually is. This reason alone is probably sufficient to explain the increase of the width from the expected $\approx 300\,\mu\text{m}$ to the observed $\approx 600\,\mu\text{m}$ width of the residuals.

CHAPTER 5

Test of Different Gas Mixtures

The standard operation of STYX is to use a gas mixture consisting of 82% Ar and 18% CO_2 and to apply a voltage of 1 850 V to its modules. This gas mixture is similar to the Ar:CO_2 mixture of 80:20 that was used in the ZEUS STT [5], but the main reason for this ratio is the price because this mixture is commercially available as a welding gas and hence relatively cheap. Unlike the ZEUS STT, STYX is not located in a collider experiment, hence the rate of particles crossing STYX is lower than for the STT. This reduces the probability that many electron-ion avalanches occur at the same time and the need to minimise the dead time. As explained in Section 2.2, both is a reason to use quenching gas. Therefore, it makes sense to test gas mixtures with less quenching gas. Here, Ar:CO_2 mixtures of 86:14 and 90:10 are tested. Using the same gases in different ratios seems promising because the characteristics of the detector may be expected to change gradually, whereas they might change fundamentally if entirely different gases are used. For instance, the drift velocity changes with different gases, which might make modifications of the readout system necessary in order to adapt it to different drift times, if the change is very strong. Moreover, there are practical reasons for Ar and CO_2: argon is cheaper than other noble gases because it is the most abundant one in the atmosphere of the Earth. Most of the commonly used quenching gases other than CO_2 are inflammable (e.g. organic quenching gases like methane etc.), which makes it difficult to test them while complying with fire safety regulations.

The main motivation to test different gas mixtures is to find out is how the detector performance changes. In particular, the detection efficiency may change, and an increase is desirable. Additionally, different characteristics, such as the *t-r* relation and the drift time spectra may change, which means that certain settings of the experiment may need to be adjusted to ensure an optimal experimental performance, depending on how drastic the changes are. The module voltage is one example of a setting that needs to be chosen such that it suits the gas mixture.

5.1 Procedure

Since the standard voltage of 1 850 V might lead to too high currents when less CO_2 than usual is used, voltages from 1 800 V to 1 850 V in steps of 10 V have been applied to the modules in order to find good operation points[1]. This has also been done for the standard gas in order to have a comparison where only the gas composition, not the voltage, differs.

[1] The reasons have been explained in Section 2.2. The quenching gas suppresses additional avalanches and noise. In the case of the tests presented here, the voltage is always similar, which means that the gas amplification is *higher* the lower the fraction of quenching gas is.

For all three gas mixtures, the way to operate the detector as part of the data taking procedure does not change intrinsically. Therefore, the lab course can be performed with all gas mixtures. The findings can differ, however. Especially, it is not a priori clear whether the threshold voltage of the front-end board needs to be changed with respect to the standard settings, because the noise and the signal height may be different with a different mixture. Also, the relation between the drift time and the distance of a track is expected to differ. In Section 5.4, this is investigated using data and in Chapter 6 using a simulation.

Since the amount of quench gas is lower in the non-standard gas mixtures, the current in the modules is higher in general. It normally is, however, still much lower than the maximum current $I_{\text{max}} = 2.0\,\mu\text{A}$ above which the module voltage automatically shuts down in order to avoid damage to the modules. Nevertheless, such a shutdown sometimes occurs, especially during long overnight data takings. It occurs most frequently at high temperatures, but a strong correlation with the voltage or gas mixture cannot be observed. The reason why high temperatures may lead to an overstepping of the maximal current is that an increase of the temperature increases the gas amplification. This is because a high temperature at a similar pressure means that the density of the gas is lower. Therefore, the mean free path of electrons and ions increases (since the molecules are further apart, according to kinetic gas theory). An increase in the mean free path means higher energies at the collision of electrons with the gas molecules. Hence, the average number of secondary ionisations increases, which results in a higher gain. Moreover, at high temperatures there may be more noise in all detector components.

5.2 Straw Mask

Since the gas amplification and the noise might differ depending on the gas mixture, it has to be investigated whether the straws are marked correctly during the calibration, or whether the calibration criteria have to be changed. To this end, the calibration is performed as usual and the straw mask is evaluated.

If different straws have a malfunction, the straw mask can look differently while the same number of straws are working. Therefore, not only the straw mask is being considered, but also the number of straws with different statuses are plotted as a function of the module voltage for different gas mixtures. This can be seen in Figure 5.2.

Apparently, the Ar:CO_2 mixture of 90:10 allows for a large number of working straws, especially at a voltage of 1 850 V. But other gas mixtures can also yield a high number of working straws. It must not be forgotten, that the exact number of working straws and the way the straw mask looks depends on many other factors, over which one does not have control.

From Figure 5.1, one can see that at voltages above 1 840 V, the number of hot straws increases while the number of ok ones decreases. This is probably because the low amount of quench gas allows for some additional discharges when the voltage is so high. This seems to suggest that the best operation mode for this gas mixture is a voltage of 1 830 V. However, at low temperatures, it may be possible that the increase in hot straws only happens at higher voltages.

Figure 5.2 shows how many straws are marked as OK in the calibration procedure. For the Ar:CO_2 mixture of 90:10, the drop at high voltages can be seen again. The mixture of 86:14 leads to a high number of working straws at all voltages except for 1 820 V and 1 830 V. The dip of ≈ 90 straws in both cases is, however, unlikely to be caused by the gas mixture. In fact, the reason seems to be a malfunction of a driver board or a connecting cable, because all straws in the left third of the top module fail at the same time. This can be seen in Figure 5.3. The problematic connection has been mended and the problem vanished. This seems to suggest that all voltages can yield a high number of working straws if this gas mixture is used.

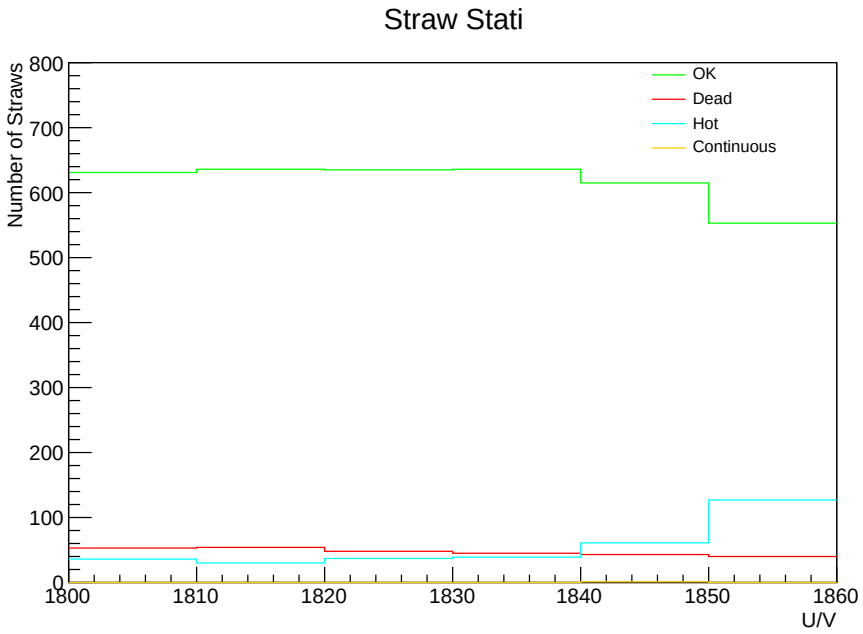

Figure 5.1: Number of straws with a respective status at different voltages for an Ar:CO_2 mixture of 90:10.

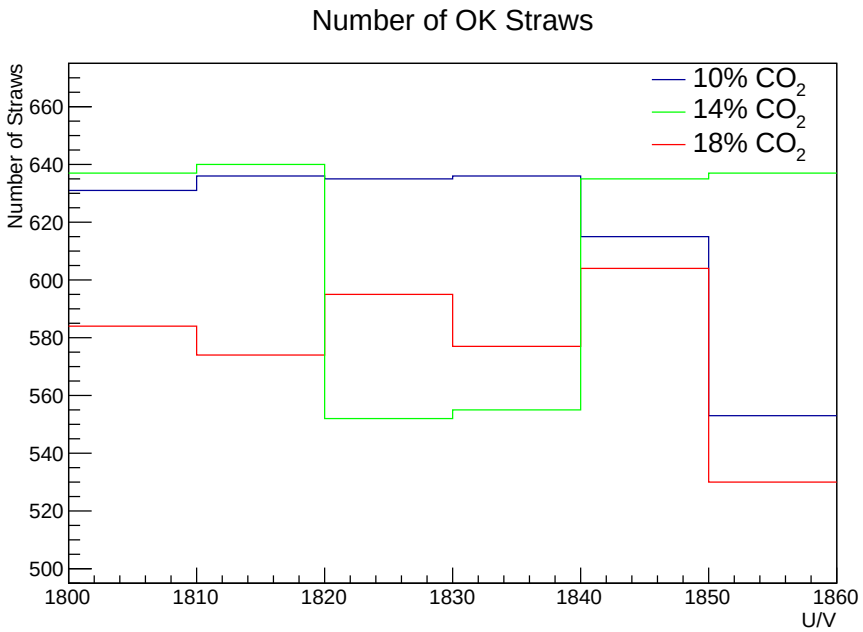

Figure 5.2: Number of working straws as a function of the voltage applied to the modules for all tested gas mixtures, indicated by their CO_2 percentage.

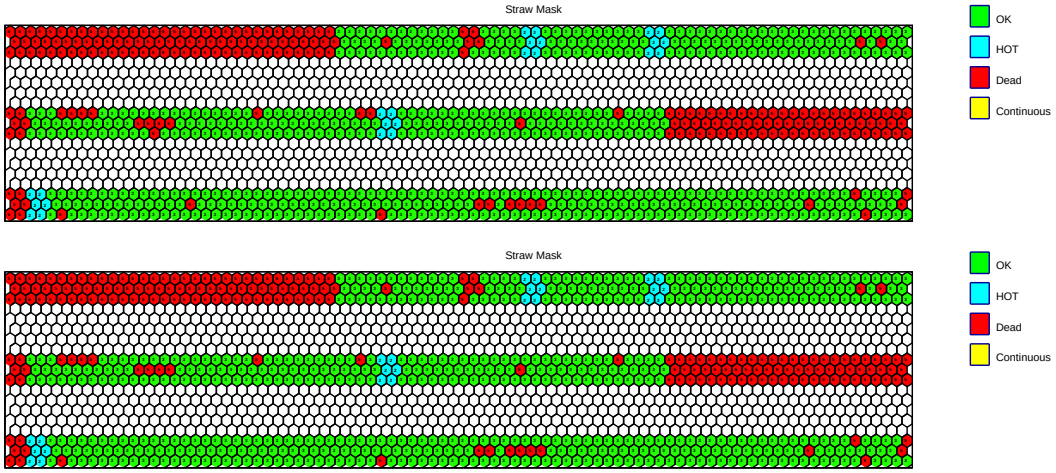

Figure 5.3: Straw masks for an Ar:CO_2 mixture of 86:14 at a voltage of 1 820 V (top) and 1 830 V (bottom).

For the standard gas mixture of 82:18, the number of working straws is somewhat lower and changes a lot. Different effects can cause this, but in general the number of dead straws is higher. This can also be due to malfunctioning channels and driver boards, or due to external conditions like the temperature. The number of straws with each status can be seen in Figure 5.4.

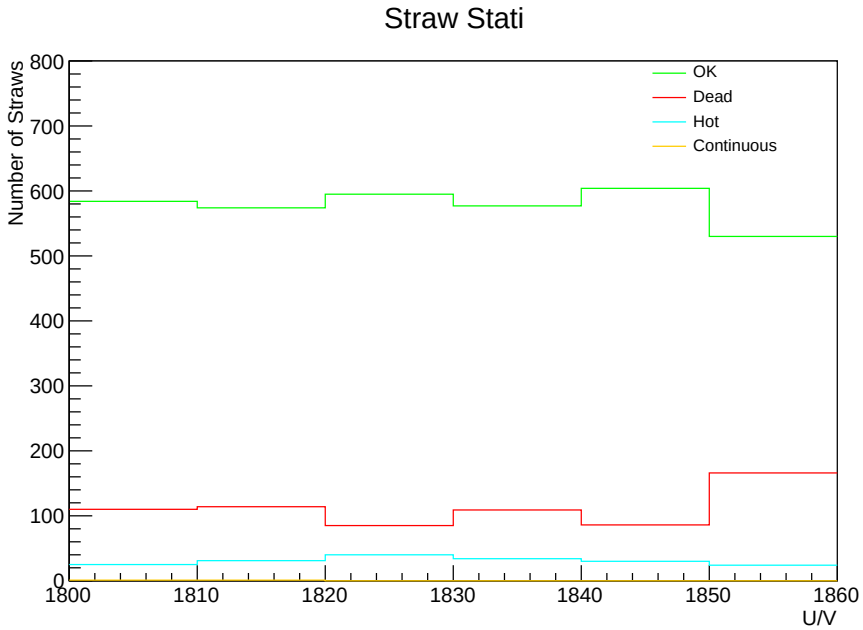

Figure 5.4: Number of straws with a respective status at different voltages for an Ar:CO_2 mixture of 82:18.

5.3 Drift Time Spectra

An interesting subject to study is the drift time spectrum of the straws. Changes in its shape might hint at differences between the different gas mixture and voltage combinations. This can be due to a different detection efficiency, gas amplification or drift velocity.

When evaluating the drift time distribution, one can consider all hits or discard those that are not on a reconstructed track. This cut may reduce the probability that a hit is only noise. Hits that are on a track are called track hits for simplicity.

Figure 5.5 shows the drift time spectra for all hits and only for track hits for four combinations of Ar:CO_2 mixtures and voltages: from top to bottom these are an Ar:CO_2 mixture of 82:18 with a voltage of 1 850 V (i.e. standard settings), 86:14 with 1 820 V, 90:10 with 1 810 V and 90:10 with 1 830 V. For the latter combination, both distributions look rather "box-like". This is what one expects if the radius of all hits follows a uniform distribution. The decrease at low drift times might be due to a lower amplification of the signal if the primary ionisation is at lower radii. At high drift times, the distribution also decreases, probably because the electric field is weakest at the exterior parts of the straw tube and does not accelerate electrons fast enough to *always* cause an avalanche that is not suppressed by the quench gas.

The deviation from a "box-like" shape is much larger for the standard settings, however. Here, one sees a flatter slope towards a peak at $\approx$ 20 ns. At higher times, the distribution has a declining shape. The absolute value of the slope increases considerably at $\approx$ 55 ns. This might hint at a stronger signal suppression due to the quench gas, but noise might be suppressed as well. However, by examining the calibrated and uncalibrated drift time spectra of single straws it can be excluded that noise is the main source of the difference. Figure 5.6 shows the drift time spectra for all straws in one layer before and after calibration for both settings. After the calibration, the drift time spectra look similar and have an amount of noise that can be neglected compared with the signal.

The Drift time spectra for an Ar:CO_2 mixture of 86:14 at a voltage of 1 820 V seems to be a transition between the two spectra described above. As for the standard settings, the trailing edge is rather flat at the beginning and becomes considerably steeper at $\approx$ 55 ns. The difference between both slopes is larger than for the standard settings, which can be interpreted as a transition towards a "box-like" shape. This also holds for the fact that the rising edge slightly is steeper than for the standard settings.

For an Ar:CO_2 mixture of 90:10 at a voltage of 1 810 V, the shape of the drift time spectrum is quite similar to the one of the same gas mixture at 1 830 V, but it is slightly trailing the range in which the latter is constant.

5.4 Space-Drift-Time Relation

As the drift time spectra suggest, the drift velocity seems to change depending on the gas mixture and voltage. This is also to be expected from a theoretical point of view. Therefore the relation between the radius of a hit and the drift time (*r*-*t* relation) needs to be investigated. To this end, a two-dimensional histogram is filled with the drift time (that can be extracted from a hit directly) on the x-axis and the radius (that is extracted from the reconstructed track) on the y-axis. An example can be seen in Figure 5.7. This plot is only made for the hits in the middle module in order to avoid a bias, because only in the middle module, tracks and drift radii are truly independent from each other. In The top and bottom module, the drift radius r_{drift} is used for the determination of the track, but r_{drift} is calculated from the drift time using the *r*-*t* relation that is already assumed in the STYX code.

For each bin in r, the mean of the drift time t and its uncertainty are extracted. The uncertainty on the mean is the standard deviation divided by $\sqrt{N}$, where N is the number of entries in each bin in r.

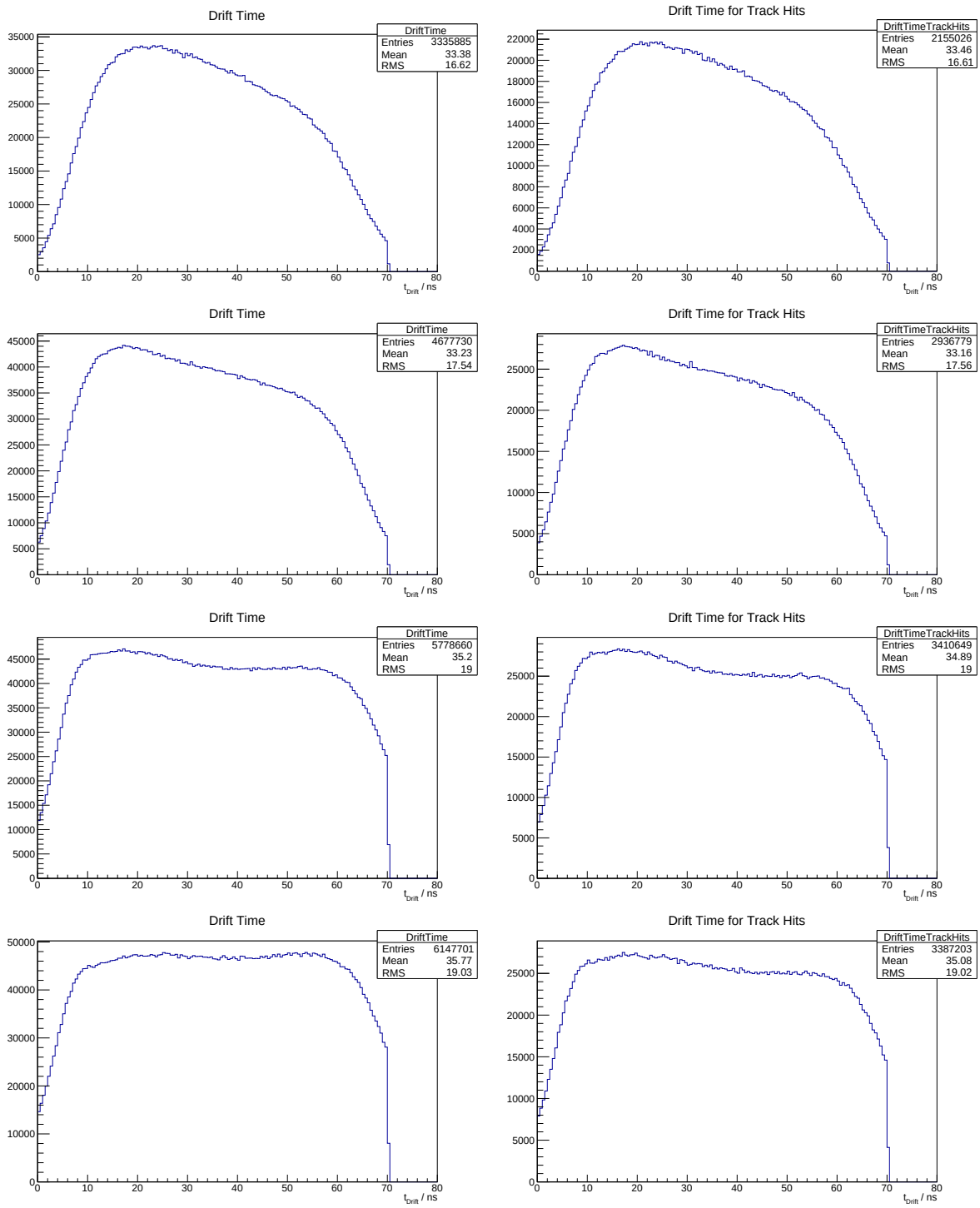

Figure 5.5: Drift time spectra for all hits (left) and track hits only (right). The Ar:CO_2 mixtures and voltages are from top to bottom: 82:18 at 1 850 V (standard settings), 86:14 at 1 820 V, 90:10 at 1 810 V and 90:10 at 1 830 V. These plots differ from those in Figure 3.2 in that they are made using a large data set to which a calibration has been applied and the spectra of all ok straws in the detector are summed up here, rather than showing the spectrum of just one straw. Differences in the number of entries between the rows are mainly due to different times for the data takings. Differences in the efficiency only cause slight differences, as will be described in Section 5.5.

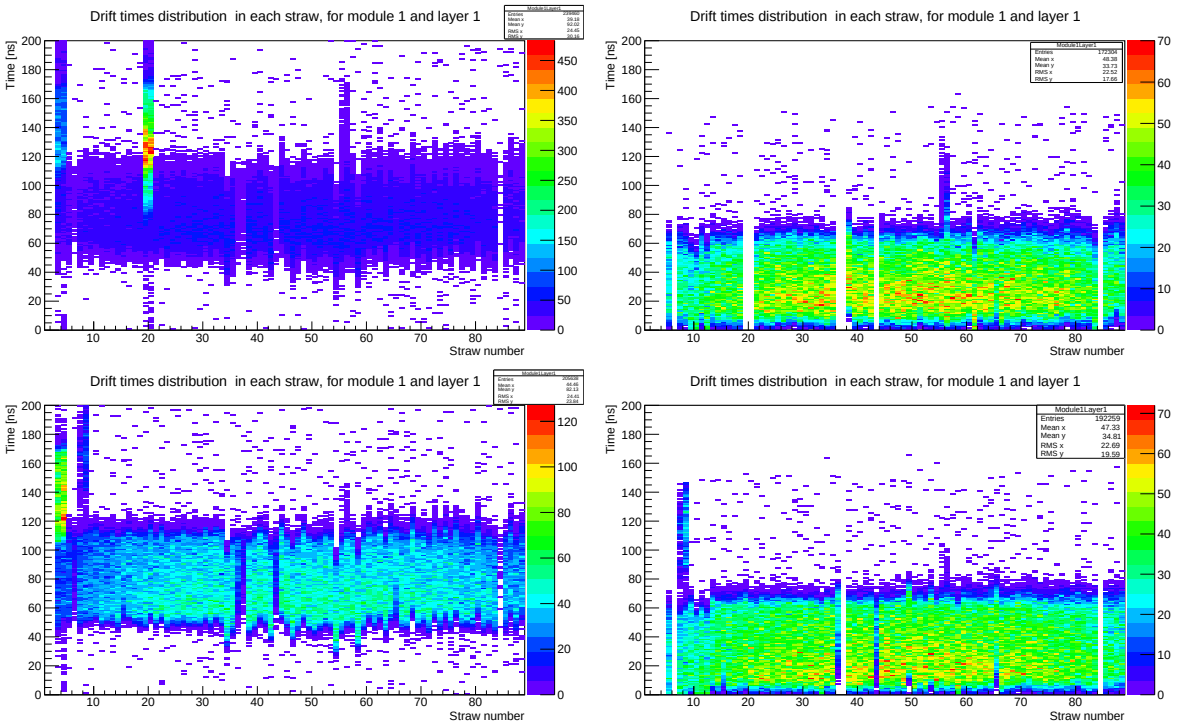

Figure 5.6: Uncalibrated (left) and calibrated (right) drift time spectra for all straws of the bottom layer of the bottom module. The top row shows the standard settings (Ar:CO_2 of 82:18, voltage 1 850 V), whereas the bottom one shows an Ar:CO_2 mixture of 90:10 with a voltage of 1 830 V.

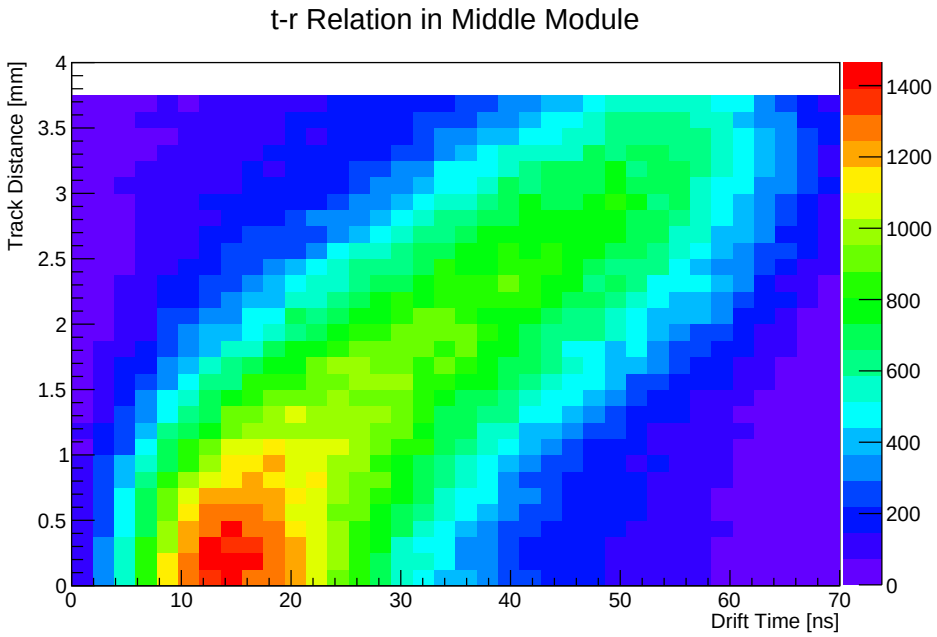

Figure 5.7: Histogram to investigate the space-drift-time relation. The x-axis contains the drift time, the y-axis the radius r that is calculated from the track. The histogram is filled with all hits in the middle module. The applied voltage is 1 850 V and the Ar:CO_2 mixture is 82:18.

The mean and its error can be plotted against the centre of the bin in r. The resulting data points are fitted with a third order polynomial. The fit to these data points is implemented with GNUPLOT. The fit polynomial is defined as

$$f(r) = p_3 \times r^3 + p_2 \times r^2 + p_1 \times r + p_0. \tag{5.1}$$

Here, f has the unit ns and r is given in mm. The coefficients p_i have the dimension time $\times$ distance^{-i}, accordingly. The reason to fit a polynomial of third order is that deviations from linearity are to be expected, hence a quadratic and cubic term seem to be sensible. Including higher powers seems to lead to an overfitting. Plotting the results seems to show that a polynomial of third order seems to be sufficient. Moreover, the implementation in the STYX code is also a polynomial of third order, which seems to be sufficient, and polynomials of the same order are more comparable.

An example for a plot of the mean and the standard deviation of t against r with a fit polynomial can be seen in Figure 5.8. Although the error-bars are relatively small, the polynomial seems to fit the data points quite well. The deviations from the expectation are similar to the one in the other cases and will be discussed together with those.

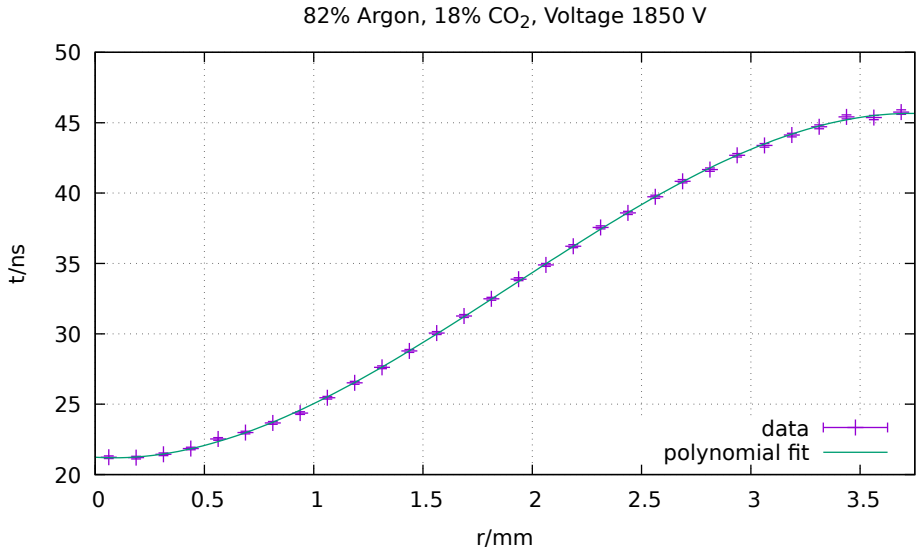

Figure 5.8: Histogram for the determination of an r-t relation extracted from data. The data values for the radius r are the bin centers of the y-axis of the histogram in Figure 5.7. The time and the error bars plotted here are the mean and the standard deviation of a one-dimensional projection of Figure 5.7 for each of its y-axis bins. A polynomial of third order has been fitted to the data points.

The resulting fit parameters for all gas mixture and voltage combinations are shown in Table 5.1 and can be compared with the values implemented in the STYX software (bottom line of Table 5.1).

It is noticeable that the parameter p_0, the y-label intersection, is in all cases much larger than the value implemented in the STYX code. One can see that the value of the parameter trends to decrease with increasing voltage and argon fraction. Only for the Ar:CO_2 mixture of 90:10 the trend is that p_0 remains constant, and at 1 850 V it increases. Such a large value of p_0 (which can also be seen from Figure 5.8) seems to be problematic, because ideally, a radius close to 0 mm also means that the drift time should be close to 0 ns, rather than having a considerable offset. The main reason for this is probably that hits with a very low radius might be underrepresented in the data. If a particle causes primary ionisations along a track that is very close to the wire, or even passes through it, the number of secondary ionisations

Table 5.1: For different Ar:CO_2 mixtures and voltages U, there are different resulting fit parameters p_i, where i refers to the power at which r contributes to the term, see Equation 5.1."STYX code" refers to the polynomial implemented in the STYX reconstruction software, converted to the units used in this chapter.

Ar:CO_2	U/V	p_0/ns	p_1/(ns/mm)	p_2/(ns/mm^2)	p_3/(ns/mm^3)
82:18	1800	17.78 ± 0.17	4.04 ± 0.37	5.33 ± 0.22	−1.019 ± 0.035
82:18	1810	16.31 ± 0.19	2.81 ± 0.41	6.25 ± 0.24	−1.138 ± 0.040
82:18	1820	16.10 ± 0.20	2.72 ± 0.43	6.33 ± 0.25	−1.150 ± 0.041
82:18	1830	15.68 ± 0.19	2.92 ± 0.40	6.20 ± 0.23	−1.130 ± 0.038
82:18	1840	15.38 ± 0.21	2.61 ± 0.44	6.54 ± 0.26	−1.180 ± 0.042
82:18	1850	14.53 ± 0.21	2.10 ± 0.46	6.83 ± 0.27	−1.200 ± 0.044
86:14	1800	14.24 ± 0.24	2.07 ± 0.52	7.56 ± 0.30	−1.358 ± 0.050
86:14	1810	12.64 ± 0.23	2.44 ± 0.49	7.44 ± 0.28	−1.325 ± 0.047
86:14	1820	13.70 ± 0.25	1.95 ± 0.53	7.69 ± 0.31	−1.372 ± 0.051
86:14	1830	12.86 ± 0.24	2.19 ± 0.51	7.65 ± 0.30	−1.360 ± 0.049
86:14	1840	11.87 ± 0.22	2.81 ± 0.47	7.28 ± 0.27	−1.297 ± 0.045
86:14	1850	11.86 ± 0.23	2.64 ± 0.51	7.36 ± 0.30	−1.308 ± 0.048
90:10	1800	11.72 ± 0.21	2.98 ± 0.46	8.04 ± 0.27	−1.488 ± 0.044
90:10	1810	11.61 ± 0.20	2.96 ± 0.44	8.08 ± 0.25	−1.496 ± 0.042
90:10	1820	11.50 ± 0.16	3.47 ± 0.36	7.56 ± 0.21	−1.407 ± 0.034
90:10	1830	11.74 ± 0.15	3.77 ± 0.32	7.30 ± 0.18	−1.368 ± 0.030
90:10	1840	11.53 ± 0.11	4.42 ± 0.24	6.72 ± 0.14	−1.266 ± 0.023
90:10	1850	13.258 ± 0.088	5.87 ± 0.19	5.33 ± 0.11	−1.052 ± 0.018
STYX code		−3.2114	27.6053	−6.43985	1.066263

might only be sufficient to cause a considerable signal above a certain drift distance (which corresponds to voltage difference with respect to the wire). Therefore such a hit might be reconstructed with slightly too large a drift radius.

The linear term of the empirical fit, i.e. the parameter p_1, is much smaller than in the code. This is probably because p_0 is relatively large. Therefore, the slope of the curve is lower, if it assumes values that are similar to the STYX code at intermediate values of r.

The quadratic and cubic terms of the polynomials fitted to the data have similar absolute values but opposite signs than in the STYX code. Parts of this can be explained with the fact that at very high radii the amount of statistics decreases and therefore the mean value can deviate.

It is moreover noticeable that high drift times do not seem to appear in the fit polynomials. Similarly to Figure 5.8, the mean drift time never seems to exceed 50 ns. This is probably due to the fact that the mean is considered and not single cases. Figure 5.5 shows, however, that drift times of up to 70 ns frequently occur. Therefore, the method of determining the r-t relation from data only seems to lead to questionable results.

The analogous method to determine the dependence of r on t (t-r relation) can be seen in Figure 5.9. The result is no less questionable, however, particularly because according to it, a drift time of 0 ns corresponds to a non-vanishing radius. All fit parameters for the t-r relation can be found in Table A.1 in Appendix A.

5.5 Efficiency

An important characteristic of the experiment is its detection efficiency for cosmic rays. To this end, one can compare tracks that are expected to be seen by the middle module with what it actually detects. Since

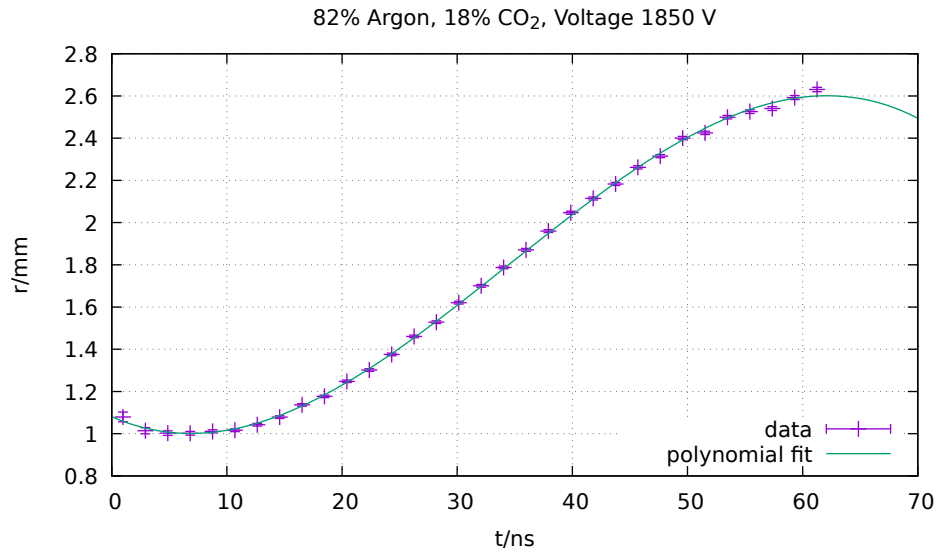

Figure 5.9: Histogram for the determination of an *t*-*r* relation extracted from data. The data values for the time t are the bin centers of the x-axis of the histogram in Figure 5.7. The radius r and the error bars plotted here are the mean and the standard deviation of a one-dimensional projection of Figure 5.7 for each of its x-axis bins. A polynomial of third order has been fitted to the data points.

the tracks are reconstructed from segments or clusters in the top and bottom module, the middle module is not involved in the track reconstruction and "observes" the tracks independently. The number of straws a track intersects in the middle module is the expected number of hits. This can be compared with the number of observed hits in those straws event by event.

Figure 5.10 shows a histogram that can be used to determine the efficiency. The x-axis shows the number of straws in the middle module that are crossed by a track, such that a hit may be expected in them. The y-axis gives the number of straws where a hit has been observed in those straws where the hits may be expected from the track. This histogram is filled event by event.

Since the track angles follow a cosinusoidal function of the zenith angle (Figure 3.6), most tracks only intersect three straws in the middle module. The second highest number of tracks crosses four straws. All other cases are very rare. The following investigations on the efficiency therefore only consider the case of three expected hits, since the statistics is the highest in this case. For three expected hits, the most frequent case is that none are observed. This is due to dead straws.

If the efficiency of a straw has the value ε (with $\varepsilon \in [0, 1]$), the probability $P(n, \varepsilon, k)$ to detect k hits on a track intersecting n straws is given by the binomial distribution as [16]:

$$P(n, \varepsilon, k) = \binom{n}{k} \varepsilon^k (1 - \varepsilon)^{n-k}. \tag{5.2}$$

Therefore, the efficiency can be calculated as

$$\varepsilon^3 = \frac{N_{\text{obs},3}}{N_{\text{exp},3}} \Rightarrow \varepsilon = \sqrt[3]{\frac{N_{\text{obs},3}}{N_{\text{exp},3}}}, \tag{5.3}$$

where $N_{\text{obs},3}$ is the number of events where three hits have been observed (analogously for $N_{\text{obs},2}$,$N_{\text{obs},1}$,

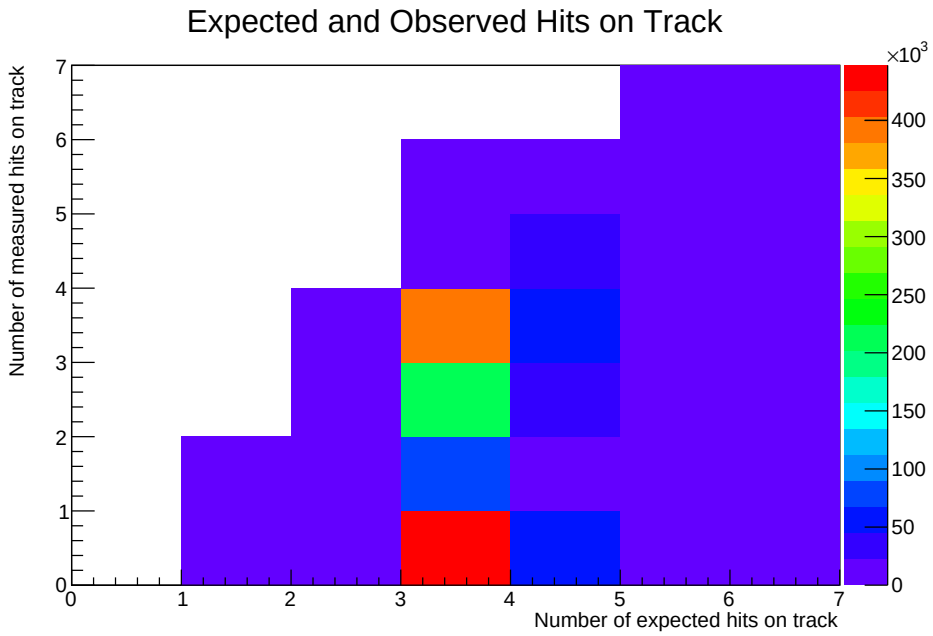

Figure 5.10: Histogram for the number of expected and observed hits in the middle module. The x-axis shows how many hits are expected in the middle module along a track, that is constructed using the top and the bottom module. The y-axis shows how many hits were observed in those straws. The histogram is filled on a event by event basis. This plot was made using an Ar:CO_2 mixture of 86:14 while applying a voltage of 1 850 V.

and $N_{\text{obs},0}$) in the straws where the three hits are expected to be in the middle module and $N_{\text{exp},3}$ is the number of events where three hits in the middle module are expected. The efficiency can also be derived from the ratio of some event probabilities, e.g.:

$$\frac{P(3,\varepsilon,2)}{P(3,\varepsilon,3)} = \frac{3\varepsilon^2(1-\varepsilon)}{\varepsilon^3} = \frac{3(1-\varepsilon)}{\varepsilon} = \frac{N_{\text{obs},2}}{N_{\text{obs},3}} \Rightarrow \varepsilon = \varepsilon_\alpha := \frac{N_{\text{obs},3}}{N_{\text{obs},3} + \frac{N_{\text{obs},2}}{3}}, \tag{5.4}$$

or, similarly:

$$\frac{P(3,\varepsilon,1)}{P(3,\varepsilon,2)} = \frac{3\varepsilon(1-\varepsilon)^2}{3\varepsilon^2(1-\varepsilon)} = \frac{1-\varepsilon}{\varepsilon} = \frac{N_{\text{obs},1}}{N_{\text{obs},2}} \Rightarrow \varepsilon = \varepsilon_\beta := \frac{N_{\text{obs},2}}{N_{\text{obs},1} + N_{\text{obs},2}}. \tag{5.5}$$

Moreover, the efficiency can also be calculated from those cases where the number of detected hits on track is 0 as:

$$P(3,\varepsilon,0) = (1-\varepsilon)^3 = \frac{N_{\text{obs},0}}{N_{\text{exp},3}} \Rightarrow \varepsilon = 1 - \sqrt[3]{\frac{N_{\text{obs},0}}{N_{\text{exp},3}}}. \tag{5.6}$$

For the following analysis, only Equations 5.4 and 5.5 are used. This is in order to receive results only from numbers that have been observed, rather than also including expected numbers. This way the impact of malfunctioning straws is reduced. In Particular, a track on which k hits are observed, crosses at least k straws without malfunction. Hence, tracks that intersect large groups of malfunctioning straws, especially the right part of the middle module (where the straws are connected to a FE board that is not connected and are therefore considered as dead, Section3.3) are excluded. Moreover, the expectation which straws a track crosses depends on the alignment of the middle module. Therefore, the number of

events where three hits have to be expected ($N_{\mathrm{exp,3}}$) may have errors that are difficult to estimate. The offset found in Chapter 4 is considered, however. Of course, the alignment and related errors also affect the number of hits where three straws are expected to show a hit and k hits are observed ($N_{\mathrm{obs,k}}$), but in the case of Equations 5.4 and 5.5, this affects both the numerator and the denominator only linearly, such that the incertitude due to alignment uncertainties does not increase as much as in a term where numbers to the third order are compared.

The uncertainty on the number of tracks with k hits when three are expected ($\Delta N_{\mathrm{obs,k}}$) is calculated under the assumption that $N_{\mathrm{obs,k}}$ follows a Poisson distribution, hence $\Delta N_{\mathrm{obs,k}} = \sqrt{N_{\mathrm{obs,k}}}$. Hence, $\Delta N_{\mathrm{obs,k}} \ll N_{\mathrm{obs,k}}$ for the orders of magnitude of $N_{\mathrm{obs,k}}$ typically observed here. This allows for a calculation of the uncertainty $\Delta\varepsilon$ on the efficiency using the Gaussian error propagation[2]. For ε_α and ε_β as defined above, the uncertainties take the following form:

$$\Delta\varepsilon_\alpha = \frac{\sqrt{N_{\mathrm{obs,2}} N_{\mathrm{obs,3}} \left(N_{\mathrm{obs,2}} + N_{\mathrm{obs,3}}\right)}}{3\left(N_{\mathrm{obs,3}} + \frac{N_{\mathrm{obs,2}}}{3}\right)^2} \tag{5.7}$$

$$\Delta\varepsilon_\beta = \frac{\sqrt{N_{\mathrm{obs,1}} N_{\mathrm{obs,2}} \left(N_{\mathrm{obs,1}} + N_{\mathrm{obs,2}}\right)}}{\left(N_{\mathrm{obs,1}} + N_{\mathrm{obs,2}}\right)^2} \tag{5.8}$$

Table 5.2: Efficiency as determined using ε_α and ε_β and the corresponding errors for all gas mixture and voltage combinations.

$Ar:CO_2$	U/V	ε_α	$\Delta\varepsilon_\alpha$	ε_β	$\Delta\varepsilon_\beta$
82:18	1800	0.6865	0.0012	0.6195	0.0019
82:18	1810	0.7564	0.0012	0.6791	0.0017
82:18	1820	0.7471	0.0011	0.6934	0.0016
82:18	1830	0.77114	0.00056	0.69295	0.00079
82:18	1840	0.7771	0.0015	0.7327	0.0020
82:18	1850	0.7953	0.0012	0.7511	0.0016
86:14	1800	0.81520	0.00079	0.7582	0.0010
86:14	1810	0.82499	0.00080	0.7330	0.0010
86:14	1820	0.8283	0.0013	0.7740	0.0016
86:14	1830	0.8455	0.0016	0.7702	0.0020
86:14	1840	0.83408	0.00099	0.7330	0.0013
86:14	1850	0.84446	0.00062	0.75899	0.00080
90:10	1800	0.83520	0.00081	0.7671	0.0010
90:10	1810	0.84080	0.00096	0.7709	0.0012
90:10	1820	0.8396	0.0015	0.7568	0.0020
90:10	1830	0.83264	0.00097	0.7539	0.0012
90:10	1840	0.8401	0.0010	0.7201	0.0013
90:10	1850	0.68425	0.00095	0.6335	0.0015

Table 5.2 contains the efficiency as determined based on Equations 5.4 and 5.5 together with the corresponding errors for all voltage and gas mixture combinations. A plot of those values can be seen in

[2] which only is an approximation, if the series decomposition of the function on which it is applied contains terms of higher order than quadratic [21].

Figure 5.11, but since the error-bars are similarly wide as the line-width, they are left out. The results indicate that the Ar:CO_2 mixture of 82:18 mostly has a lower efficiency than the other two. The difference in efficiency between the Ar:CO_2 mixtures of 82:18 and 90:10 is not very big, however.

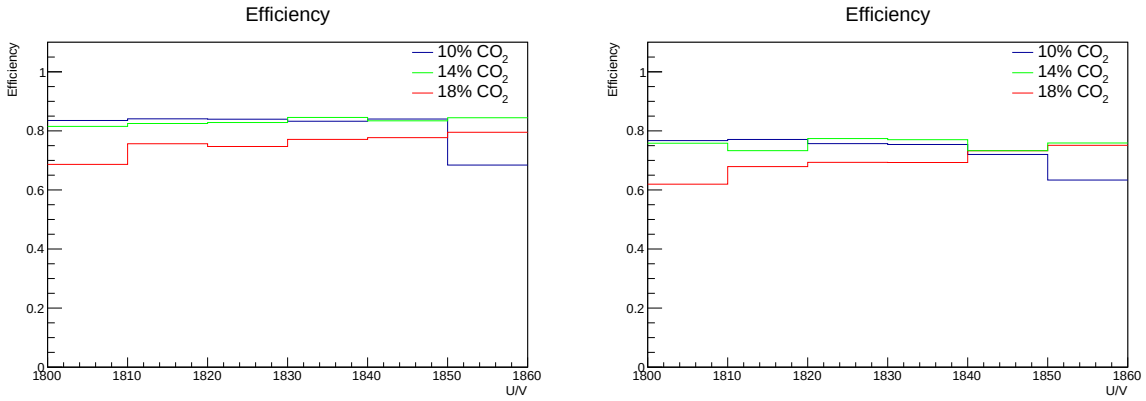

Figure 5.11: Plot of the Efficiency depending on the gas mixture (given as CO_2 percentage) and the Voltage. The left histogram contains the efficiency as measured using ε_α, the right one ε_β. Since the error-bars are similarly wide as the line-width, they are not included in the plot.

For the Ar:CO_2 mixture of 82:18, a strong increase of the efficiency can be observed as the voltage increases. At 1 850 V (the normal operation mode) an efficiency between 75 and 80 % is achieved.

For the Ar:CO_2 mixture of 86:14, the increase of the efficiency with the voltage is very moderate and seems to cease or even slightly reverse at $\approx$ 1 830 V. It should not be forgotten, that the efficiency is already at the lowest voltage (1 800 V) higher than for all cases with the standard gas mixture. The reason why too high a voltage can lead to a drop of the efficiency is that straws might change their status from "ok" to "hot" or "continuous", or at least that the noise increases in them, because the low amount of quench gas is not sufficient to suppress the noise. For the Ar:CO_2 mixture of 90:10 an increase in the number of hot straws can be seen in Figure 5.1.

In the case of the Ar:CO_2 mixture of 90:10, efficiencies that are as good as those for the mixture of 86:14 can be achieved. However, at $\gtrsim$ 1 840 V, a strong drop of the efficiency occurs, such that it assumes a very low value at 1 850 V. This is because the number of hot straws increases drastically at high voltages when this gas mixture is used. This can also be seen from Figure 5.1.

One problem must not be ignored, however: the values for ε_α is always higher than the ε_β. The difference mostly is as big as $\approx$ 7 to 8 percentage points. This is almost two orders of magnitude larger than the uncertainties $\Delta\varepsilon_\alpha$ and $\Delta\varepsilon_\beta$. Although this does not prove that those uncertainties are too small, it strongly suggests that. What is even more likely is the conjecture that there is an error in the underlying assumptions that went into the determination of the efficiency, such that the methods to determine ε_α and ε_β are inconsistent with each other. The quantity ε_α can be overestimated if $N_{\text{obs},3}$ is overestimated, or if $N_{\text{obs},2}$ is underestimated. Additionally, ε_β can be underestimated if $N_{\text{obs},2}$ is underestimated or $N_{\text{obs},1}$ is overestimated. The case of an underestimate of $N_{\text{obs},2}$ can happen, if the third observed hit is actually caused by noise rather than the actual cosmic particle. In other words, if the particle only causes an observable hit in two of the three straws it crosses, and a hit due to noise happens in the third straw at the same time, the track, which should be counted as "two observed while three expected" is counted as "three observed while three expected" Hence, this case also leads to an overestimate of $N_{\text{obs},3}$. However, this case is not very likely[3]. Moreover, a distinction between a hit on track due to "actual" ionisation from

[3] One may also argue that using the same argument, $N_{\text{obs},2}$ could be overestimated, if only one hit is actually caused by the

the particle and a hit on track due to noise cannot be made and leads to deeply philosophical questions about causality, which should not be considered by a physicist[4]. A more promising explanation is the possibility of a correlation between different straws in one readout channel. Since the six straws in a channel are grouped in three layers with two straws next to each other, it is impossible that a track crossing only three straws can cross straws in three different channels. Cross-correlations inside a channel can be assumed from almost every straw mask, because they almost always feature groups of six straws that are dead or hot and that are grouped in the same way as the straws belonging to one channel. Figures 3.4, 5.3, 7.2 and 7.3 display some examples. Since there are correlations between the straws, the underlying assumption that the binomial distribution can be used is only an approximation. If a straw registers a hit with increased probability when two other straws in the channel observe a hit, this will also shift events from "two observed while three expected" to "three observed while three expected".

5.6 Recommendation for Gas Mixture and Voltage

Table 5.2 shows the efficiency achieved with all gas mixture and voltage combinations. If the default Ar:CO_2 mixture is used, the voltage should not be lower than 1 850 V because that would decrease the efficiency. Every reduction of the voltage by 10 V leads to a loss of efficiency of several percent points. Both the Ar:CO_2 mixtures of 86:14 and 90:10 can lead to an increased efficiency. Using the former, the highest efficiency is obtained at 1 820 V or 1 830 V, depending on whether the quantity ε_α or ε_β is considered. For the Ar:CO_2 mixture of 90:10, the voltage should not exceed 1 830 V. The highest efficiency with this gas mixture is achieved at a voltage of 1 810 V. The drift time spectrum for this gas mixture and 1 830 V is somewhat more constant at intermediate times, which seems advantageous because this suggests the efficiency is less dependent on the drift radius in this case.

particle and another one is caused by noise. This case is, however less likely than the other one, because $N_{\mathrm{obs},1}$ is considerably lower than $N_{\mathrm{obs},3}$.

[4] The reader who is so inclined may consider different causes for ionisation in the light of different theories of causality as presented in [22]. Some of those theories might not even be sensitive to the distinction mentioned above.

CHAPTER 6

Monte Carlo Simulation

As already mentioned in Section 5.4, changing the gas mixture and the voltage will also change the drift velocity and the gas amplification. Therefore, the *t*-*r* relation needs to be modified. In order to find the correct formula, a Monte Carlo simulation is performed with Garfield++ [23].

A straw is simulated with the correct radii of the tube (3.7475 mm) and the wire (25 µm). It is filled with Ar:CO_2 mixtures of 82:18, 86:14 and 90:10 in the respective simulations. The voltage between the wire and the tube is set in the range from 1 800 V to 1 850 V in steps of 10 V. Therefore, 18 combinations of gas and voltage are considered. For each gas and voltage combination, several points of primary ionisation at a starting time $t = 0$ ns are simulated, and the time of the signal is observed. In order to average over statistical fluctuations, the simulation is repeated 1000 times for each point. [1] This allows for the determination of the mean and its standard deviation of the drift time for a given radius. The points of primary ionisation are distributed in a range from 50 µm to 3 740 µm in steps of 205 µm. This corresponds to equidistant steps from near the wire to neat the tube. A cubic polynomial is fitted to the distribution of points. The reason for this is the same as in Section 5.4: the deviations from a linear function seem small, but not negligible, and a comparison with the STYX code and the *r*-*t* relation from data is easier if all polynomials have the same degree.

Like for data, the fit to the simulation data points is implemented with gnuplot. The fit polynomial is defined as in Equation 5.1

The fit results for the *r*-*t* relation extracted from the Monte Carlo simulation can be found in Table 6.2 for all gas mixtures and voltages. It is noticeable that the linear term often comes with smaller relative errors on the coefficient than the other ones. Moreover, given that the radius r can assume values from 25 µm to 3 747.5 µm, the linear term contributes dominantly.

Comparing the result found for an Ar:CO_2 mixture of 82:18 and a voltage of 1 850 V with the polynomial used in STYX so far seems to show some discrepancy if one only considers the values of the coefficients. The linear term is about twice as big in the STYX code and the quadratic term has a larger absolute value and is negative. Moreover, the constant in the polynomial is lower and the cubic term larger with a positive value, rather than a negative one. Plotting both functions, however, reveals that both have relatively similar values in the range that is to be considered here, which is between the wire and the tube (25 µm to 3 747.5 µm). This can be seen in Figure 6.2. The reason is that many differences cancel each other, e.g. the relative sign and value of the linear and quadratic term. For most of the range, namely if $r \gtrsim 200$ µm, the fit result yields somewhat smaller drift times than the STYX code does for

[1] If 1000 primary ionisations were simulated at the same time, the avalanches would influence each other, e.g. due to space charge effects. Therefore, the event is cleared every time and each simulation starts under the same initial conditions, in particular in a gas without ions.

Table 6.1: Values of the parameters given to the simulation programme Garfield++. These may help to reproduce the simulation. The CO_2 fraction is set such that it adds up to unity with the Ar fraction. The gas temperature is chosen as 293.15 K = 20 °C because this is similar to the room temperature over a large time of the year. On warm summer days, it is significantly exceeded, but even in summer the night temperatures are not very much higher. The gas pressure inside STYX is not known and can only be estimated. From the fact, that the gas slowly flows through a bubbler, producing bubbles of a few cm^3, it can be seen that the gas pressure is slightly higher than room pressure (which also changes with time). The standard atmosphere is 1.01325 bar = 760 Torr [12]. Therefore the simulation is once performed assuming a pressure of 1.1 bar = 825.1 Torr and once 1.0066 bar = 755 Torr. These values can be regarded upper and lower bound: the lower bound would only exceed the pressure of the room under the influence of a low-pressure area, whereas the upper bound would exceed the pressure of the room greatly, even under the influence of a high-pressure area. The differences in the drift times between both cases are found to be negligible.

quantity	value	unit
wire radius	0.0025	cm
tube radius	0.37475	cm
tube length	20	cm
wire voltage	{1800, 1810, 1820, 1830, 1840, 1850}	V
tube voltage	0	V
Ar fraction	{82, 86, 90}	%
CO_2 fraction	{18, 14, 10}	%
gas temperature	293.15	K
gas pressure	{755.0, 825.1}	Torr
radius of ionisation	$50 + n \times 205, n \in \{0, 1, ..., 18\}$	µm

Table 6.2: Resulting fit parameters for different Ar:CO_2 mixtures and voltages. The indices of the coefficients correspond to the power of the term in radius r. "STYX code" refers to the polynomial implemented in the reconstruction software of STYX, converted to the units used in this chapter.

Ar:CO_2	U/V	p_0/ns	p_1/(ns/mm)	p_2/(ns/mm^2)	p_3/(ns/mm^3)
82:18	1800	-1.06 ± 0.17	13.81 ± 0.40	1.14 ± 0.25	$(-9.4 \pm 4.3) \times 10^{-2}$
82:18	1810	-1.08 ± 0.19	13.92 ± 0.44	1.07 ± 0.27	$(-8.5 \pm 4.7) \times 10^{-2}$
82:18	1820	-1.06 ± 0.18	13.85 ± 0.42	1.08 ± 0.26	$(-8.4 \pm 4.5) \times 10^{-2}$
82:18	1830	-1.04 ± 0.17	13.75 ± 0.40	1.17 ± 0.25	$(-10.4 \pm 4.3) \times 10^{-2}$
82:18	1840	-1.06 ± 0.18	13.81 ± 0.41	1.10 ± 0.25	$(-8.8 \pm 4.4) \times 10^{-2}$
82:18	1850	-1.08 ± 0.19	13.85 ± 0.44	1.11 ± 0.27	$(-9.5 \pm 4.7) \times 10^{-2}$
86:14	1800	-1.11 ± 0.17	14.73 ± 0.40	1.71 ± 0.25	$(-24.1 \pm 4.2) \times 10^{-2}$
86:14	1810	-1.13 ± 0.19	14.77 ± 0.44	1.69 ± 0.27	$(-24.0 \pm 4.7) \times 10^{-2}$
86:14	1820	-1.10 ± 0.16	14.67 ± 0.37	1.75 ± 0.23	$(-25.0 \pm 4.0) \times 10^{-2}$
86:14	1830	-1.07 ± 0.15	14.48 ± 0.35	1.88 ± 0.22	$(-27.2 \pm 3.8) \times 10^{-2}$
86:14	1840	-1.10 ± 0.16	14.58 ± 0.38	1.78 ± 0.23	$(-25.0 \pm 4.0) \times 10^{-2}$
86:14	1850	-1.10 ± 0.16	14.54 ± 0.37	1.82 ± 0.23	$(-25.9 \pm 3.9) \times 10^{-2}$
90:10	1800	-1.31 ± 0.21	16.58 ± 0.49	2.10 ± 0.30	$(-31.8 \pm 5.2) \times 10^{-2}$
90:10	1810	-1.33 ± 0.21	16.59 ± 0.50	2.10 ± 0.31	$(-30.5 \pm 5.3) \times 10^{-2}$
90:10	1820	-1.34 ± 0.22	16.52 ± 0.52	2.18 ± 0.32	$(-32.5 \pm 5.6) \times 10^{-2}$
90:10	1830	-1.40 ± 0.23	16.78 ± 0.53	2.00 ± 0.33	$(-29.2 \pm 5.7) \times 10^{-2}$
90:10	1840	-1.32 ± 0.21	16.39 ± 0.49	2.28 ± 0.30	$(-34.5 \pm 5.3) \times 10^{-2}$
90:10	1850	-1.37 ± 0.22	16.52 ± 0.52	2.16 ± 0.32	$(-31.8 \pm 5.6) \times 10^{-2}$
STYX code		−3.2114	27.6053	−6.43985	1.066263

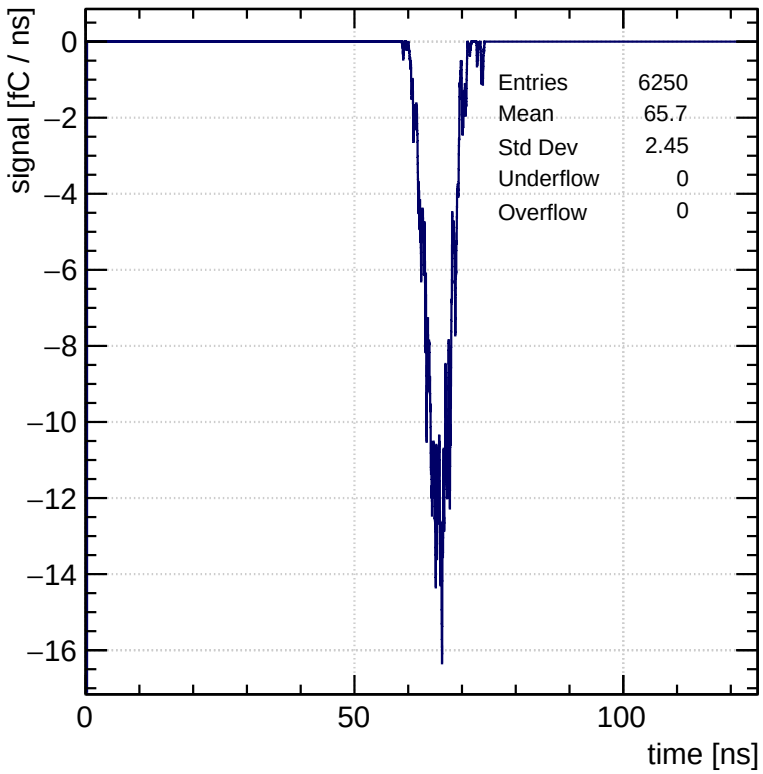

Figure 6.1: For a fixed drift radius, here 3.33 mm, 1000 primary ionisations are simulated. The respective signals are added up and plotted here. The diagram contains the current at the electrodes (in fC/ns) as a function of the time (in ns). The mean and standard deviation of this histogram give one point for fitting a polynomial. In this case, the simulated gas is an Ar:CO_2 mixture of 90:10 and the voltage is 1 830 V.

the same radius. Since not all assumptions that went into the simulation resulting in the STYX code are known, the reasons for the discrepancy are not known.

For the purposes of the experiment, the inverse relation is also very important, namely converting a drift time to a radius (*t*-*r* relation). The corresponding fits of cubic polynomials have also been implemented. The fit parameters can be found in Table A.2 of Appendix A.

In Figure 6.3, one can see that the discrepancy between the STYX code and the polynomial found for the standard settings (Ar:CO_2 mixture of 82:18, 1 850 V) in this simulation is very large for the *t*-*r* relation as well.

A comparison of the *t*-*r* relation for an Ar:CO_2 mixture of 90:10 at a voltage of 1 850 V shows a better agreement with the polynomial that has been implemented in STYX than the standard mixture in Figure 6.4. This is very surprising because the simulation resulting in the STYX polynomial assumed an Ar:CO_2 mixture of 80:20 [5]. However, a very good agreement cannot be seen here, especially at low drift times/radii. An intersection of both graphs at ≈ 40 ns, or $r_{\text{drift}} \approx 2$ mm, can be seen.

Since the fit parameters found here differ from the ones used in STYX so far, they should be adjusted according to the gas mixture and voltage. The discrepancies are particularly large in the case of the standard settings, which suggests the need for changes is especially high, if the Ar:CO_2 mixture of 82:18 is still used in the future. Investigating impact of an adjusted *t*-*r* relation on the track reconstruction seems to be a promising study as part of future bachelor's or master's theses.

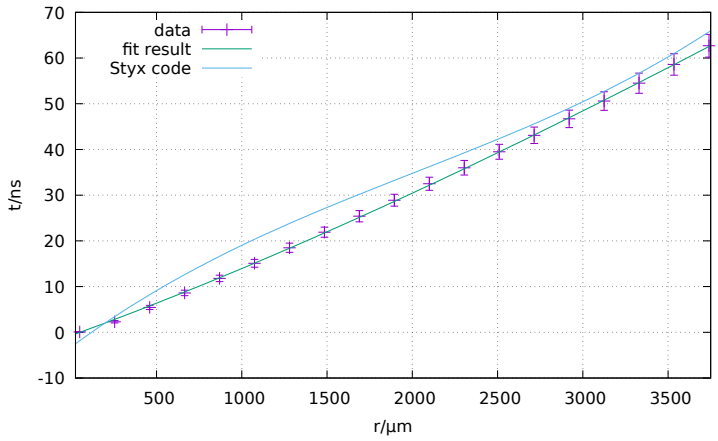

Figure 6.2: Plot of the polynomial for the *r*-*t* relation found here as a fit result for an Ar:CO_2 mixture of 82:18 at a voltage of 1 850 V and the polynomial implemented in the code of STYX so far. The range of the radius corresponds to the wire and tube radius of a straw.

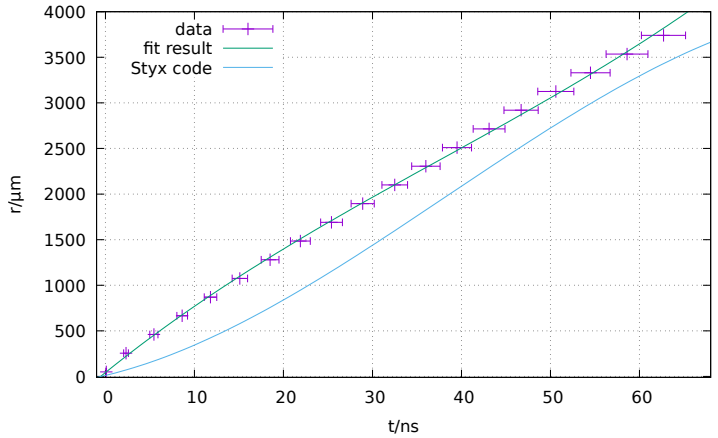

Figure 6.3: Plot of the polynomial for the *t*-*r* relation found here as a fit result for an Ar:CO_2 mixture of 82:18 at a voltage of 1 850 V and the polynomial implemented in the code of STYX so far.

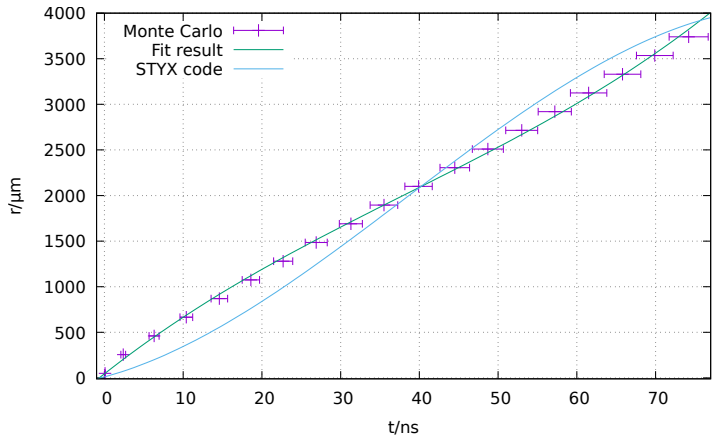

Figure 6.4: Drift times and corresponding radii for an Ar:CO_2 mixture of 90:10 and a voltage of 1 850 V with a polynomial fit to the Monte Carlo points and the relation implemented in the STYX code.

CHAPTER 7

Calibration Studies

A calibration needs to be applied to every data set in order to get proper results in the subsequent analysis. The calibration (Section 3.4.2) requires a certain number of events that must not be used in the analysis, which would be biased otherwise. Investigating how many events are necessary for the calibration may help to use more data in the analysis, if the time for data taking is constrained. The other way around, it might help to determine how many events are at least needed for a data taking, which corresponds to how much time is needed. This might help to make the time schedule for the Advanced Lab Course more flexible.

7.1 Number of Events Used for Calibration

The lab course manual for STYX recommends to use 300 000 events for the calibration of one overnight data taking. This number refers to the number of events that are given to StyxM2C2 as an input parameter. Since StyxM2C2 discards all empty events, the number of remaining events is somewhat lower and varies with the number of working straws and the detection efficiency. Given that a typical night of data taking yields more than a million events, one still has enough events remaining to perform a thorough data analysis. Nevertheless, the question how many events are necessary for calibration is relevant, especially if one wants to calibrate shorter data samples. In this case, one should not lose too many events for the calibration.

The reason why a large number of events is needed for calibration is its method. As described in Section 3.4.2, a line is fitted to the raising slope of the drift time spectrum of each straw to remove its time offset and properly measure its drift time. In order to have a clear signal that stands out from the noise, a large number of hits per straw is needed (typically some thousands of hits) and there are 792 straws. Note that one event normally contains at least five hits, otherwise it is discarded as empty. If the calibration is performed with a small number of events, many straws are marked as continuous rather than another status which they have if more events are used. A straw mask that was created using a data set of 50 000 events can be seen in Figure 7.2. Figure 7.3 was created from the same data taking, but 300 000 events were used. One sees that all straws that seem to be continuous in Figure 7.2 are actually working.

In order to get a systematic overview over the behaviour of the straw mask when differently many events are used, a calibration is performed on the same data set using 50 000 to 500 000 events in steps of 50 000. The number of all straw stati is plotted as a function of the number of events. The resulting histogram is produced for several situations, especially one where relatively many straws work and one where relatively few do. The histograms can be seen in Figure 7.4.

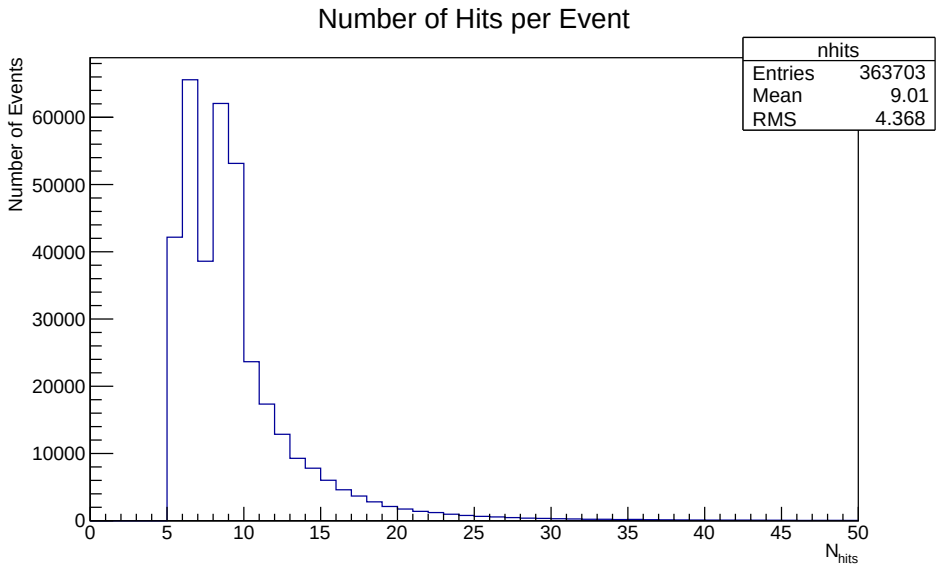

Figure 7.1: Number of hits per event for an overnight data set. At least five hits are needed to construct a track, as explained in Section 3.4.3, therefore events with less hits are discarded by StyxM2C2 (Section 3.4.1). Therefore they are not filled into the histogram.

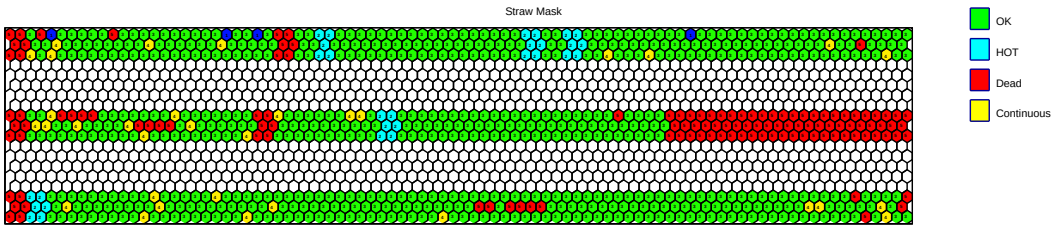

Figure 7.2: Example of a straw mask that was created using 50 000 events. A relatively large number of straws is marked as continuous.

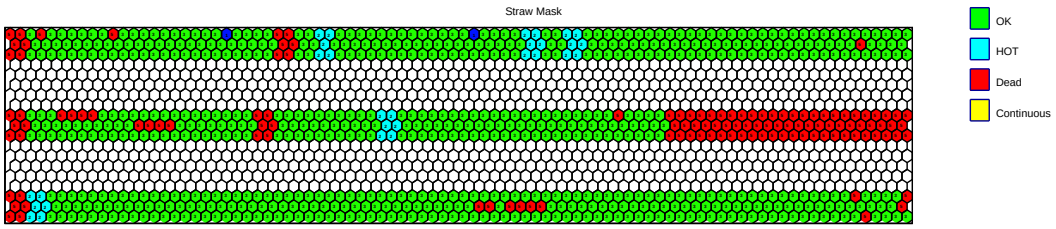

Figure 7.3: Straw mask created from 300 000 events in the same data taking as Figure 7.2. Most of the straws that seem continuous there prove to be working. Note that this is a straw mask with quite few malfunctioning straws.

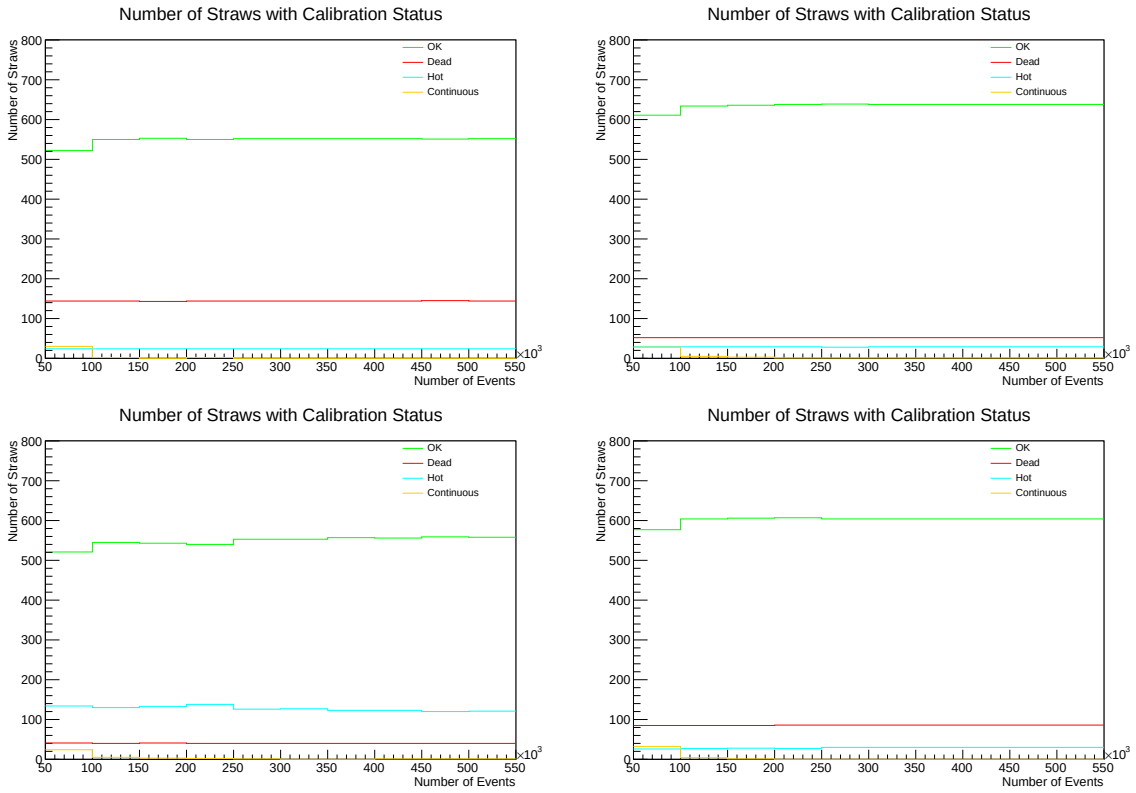

Figure 7.4: Numbers of straws with a certain status depending on the number of used events. The data of each histogram has been taken with different settings (gas mixture and voltage) and possibly under different external circumstances, in particular temperatures, which is the reason why the numbers converge to different values in each histogram.

In general, the number of continuous straws (amber) decreases as more events are used. The number of dead (red) and hot (light blue) straws is relatively constant. Only the number of working straws (green) increases. This can be explained if working straws are not identified as such if the number of hits is too low, but they are not misidentified as dead or hot. A misidentification as dead is unlikely because a working straw does not have no hits at all as long as the number of events is not extremely low ($\ll 50\,000$). A hot straw also has a different signature, especially that the number of hits is much larger than for a working one and that the drift time spectrum is wider. In very small data sets, statistical fluctuations might result in some straws having considerably more hits than the average, but at 50 000 events the average number of hits is high enough to make this rather unlikely. Moreover, the width of the drift time spectrum does not change with the statistics. Since the working straws always constitute the largest fraction, most of the continuous straws are actually working, assuming that all identifications as continuous do not give the true status of a straw. Labelling a dead straw falsely as continuous seems somewhat disfavoured, probably because the number of hits in a dead straw is only rarely different from zero.

7.2 Conclusions and Recommendations

The question how many events are necessary for a correct calibration can be answered from the number of events in Figure 7.4 from which the number of working straws does not increase further. A 100 000 events seems already sufficient to only have so few false identifications that they can be tolerated. This should be considered especially if the number of events is so low that losing some tens of thousands of events for the subsequent analysis would be detrimental to the final results. If the number of events is so high, that any loss can be accepted, at least 200 000 events should be used in the calibration, because above this number the numbers of straws almost cease from changing.

If a calibration using a low number of events is truly required, a possible workaround might be to declare all continuous straws as working. Although this can cause some false identifications, their number does not seem high.

CHAPTER 8

Summary and Conclusions

The studies carried out for this thesis give rise to results that can improve the experiment's performance.

After describing the physical background of STYX, namely cosmic radiation and the working principles of detector components in Chapter 2, the experimental setup of STYX is explained in Chapter 3.

The studies of the alignment carried out in Chapter 4 yield the result that the middle module has an offset of $x_{\text{offset}} = -0.6\,\text{mm}$ with respect to the other two. This offset is considered in the analysis software since its determination. The width of the residuals and the deviations from a truly Gaussian shape show that the detector resolution is lower than in an ideal case. With the ZEUS STT, a resolution of $\approx 200\,\mu\text{m}$ to $\approx 300\,\mu\text{m}$ was achieved [5].

Testing different gas mixtures as described in Chapter 5 yields various results relating to the experimental performance. The number of working straws may change with the voltage and gas mixture, but the external circumstances, especially the temperature and malfunctions of the electronics, can play a considerable role (Section 5.2). In general, for all gas mixtures a high number of working straws can be achieved, if the applied voltage is suitable. It is notable that the number of working straws decreases while the number of hot ones increases at voltages beyond 1 830 V if an Ar:CO_2 mixture of 90:10 is used.

Changes in the drift time spectrum may also be observed for different voltages and gas mixtures (Section 5.3). In all cases, a space-drift-time relation can be determined from data (Section 5.4). The results for the fit parameters seem somewhat questionable, however. Especially the fact that a vanishingly low drift time corresponds to a non-vanishing drift radius (and vice versa) is probably unphysical. A shortcoming of the method mainly causing the questionable results is that both considered quantities (t_{drift} and $|d_{\text{track}}|$) are positive definite, such that their mean can be increased by events where one of them is high while the other is low. Errors in the calibration, misalignments that cannot be investigated in the current experimental setup (e.g. a torsion of the middle module with respect to the other two) and the limited detector resolution can deteriorate the results as well.

The efficiency is determined for all tested gas mixtures and voltages with the two variables ε_α and ε_β (Section 5.5). Although there is a discrepancy between them, it is demonstrated that the efficiency depends on the gas mixture and the voltage. For the Ar:CO_2 mixture of 82:18, the trend is that the efficiency increases with the voltage in the range from 1 800 V to 1 850 V. In the case of the Ar:CO_2 mixture of 86:14, the efficiency is nearly constant with respect to the voltage, whereas for the Ar:CO_2 mixture of 90:10, a drop of the efficiency can be observed at voltages $\geq$ 1 840 V. For both, the mixture of 86:14 and 90:10, the efficiency increases by some percentage points, as long as the right voltage is applied. Table 5.2 shows that the efficiency, as parametrised by ε_α, has a maximum for an Ar:CO_2 mixture of 86:14 and a voltage of 1 830 V, whereas ε_β is the highest for the same mixture and 1 820 V. However, there are several other voltages at which ε_α and ε_β are only slightly lower, both for the Ar:CO_2

mixture of 86:14 and 90:10.

The decision which gas mixture will be used in the future should also consider some other factors, of which the following three seem to be particularly important. Firstly, the prices for different mixtures may differ. Secondly, STYX and a drift chamber experiment from the bachelor lab course depend on the same gas system. If the drift chamber cannot be operated with a certain gas mixture which is used in STYX, separate systems need to be installed. Thirdly, the possible benefit from an increased efficiency should be considered. The big data samples, which are taken overnight, usually contain more than a million events. Even if half of them would be discarded, the data sample would still be sufficiently large for a typical students' analysis. Nevertheless, the time needed for data taking cannot be reduced to a time that would make an overnight data taking unnecessary. Therefore, an increase in the efficiency makes the data sets larger, but the increase in size is not crucial for the students' analysis. One thing that does change with an increase in the efficiency is the amount of non-empty events in the small data sets that are taken in order to determine the threshold voltage of the front-end boards (see Section 3.5). If the efficiency increases, this step may either be performed in a slightly shorter time, or with slightly more, and accordingly better, data.

In Chapter 6, the results of a simulation to determine a space-drift-time relation are presented. For many gas mixture and voltage combinations, in particular for the standard one, which is an Ar:CO_2 mixture of 82:18 and a voltage of 1 850 V, the simulation shows considerable discrepancies with respect to the polynomial used in the STYX software to date.This means that the code should be changed accordingly, particularly if the standard gas mixture and voltage is still used in the future. But also at other gas mixture and voltage combinations, the fit functions determined in Chapter 6 differ somewhat from the software used so far, which should therefore be modified as well if those gas mixtures are used. A merit of this thesis is, hopefully, that the parameters are available from it and can be inserted without carrying out another simulation.

The studies on the calibration described in Chapter 7 show that the number of straws with a certain status does not change drastically with the number of events used, if this is larger than 100 000. Therefore, using a data sample of 100 000 events for the calibration may be enough for a sufficient calibration. Slight changes at higher event numbers can be observed, however, such that 200 000 is probably the lowest number of events from which one can expect a result with almost vanishingly low differences with respect to a calibration with 300 000 to 500 000 events.

A possible study as part of future bachelor's or master's theses on the STYX experiment might be to investigate the impact of a modified space-drift-time relation on the residuals and the track reconstruction. Moreover, different gas mixtures may be tested, if the budget allows for that, and simulations may be carried out accordingly. For instance, one might substitute argon by another noble gas, e.g. neon. In this case, the drift velocity might increase, which might be disadvantageous as this reduces the time resolution. Nevertheless, this might be compensated if an appropriate voltage is applied. As long as such a test has not been carried out, the scepticism about other noble gases is rather speculative, which makes it worthwhile to test. Additionally, different quenching gases than CO_2 might be tested, provided that this is feasible without violating fire safety regulations.

There are also possibilities for software developments, such as including the middle module in the track reconstruction, or to change the method of track reconstruction fundamentally, e.g. using a Hough transform. A study towards this has already been carried out as a bachelor's thesis [24], however the resultant algorithm has not been implemented in the software of STYX so far.

Bibliography

[1] B. Valeriani-Kaminski, *physics601 - Physikalisches Institut Universität Bonn*, URL: https://www.praktika.physik.uni-bonn.de/module/physics601 (cit. on p. 1).

[2] *Master in Physics - Fachgruppe Physik/Astronomie*, URL: https://www.physik-astro.uni-bonn.de/studies/study-courses-1/master-in-physics?set_language=en (cit. on p. 1).

[3] *E217 STYX*, URL: https://www.praktika.physik.uni-bonn.de/module/physics601/downloads/experiments/e217e (cit. on p. 1).

[4] P. Seema, *Straw Tube Young Student eXperiment - STYX*, 2015, URL: https://www.brock.physik.uni-bonn.de/research/styx-experiment (cit. on p. 1).

[5] S. Fourletov, *Straw tube tracking detector (STT) for ZEUS*, Nuclear Instruments and Methods in Physics Research Section A: Accelerators, Spectrometers, Detectors and Associated Equipment **535** (2004) 191, Proceedings of the 10th International Vienna Conference on Instrumentation, ISSN: 0168-9002, URL: http://www.sciencedirect.com/science/article/pii/S0168900204016006 (cit. on pp. 1, 21, 25, 41, 47).

[6] C. Grupen et al., *Astroparticle Physics*, 1st ed., Springer-Verlag, 2005 (cit. on pp. 3, 4, 14).

[7] C. Patrignani et al., *Review of Particle Physics*, Chin. Phys. **C40** (2016) 100001 (cit. on pp. 4, 5).

[8] M. Tanabashi et al., *Review of Particle Physics*, Phys. Rev. D **98** (3 2018) 030001, URL: https://link.aps.org/doi/10.1103/PhysRevD.98.030001 (cit. on pp. 4, 6, 14).

[9] W. R. Leo, *Techniques for Nuclear and Particle Physics Experiments – A How-to Approach*, 2nd ed., Springer-Verlag, 1994 (cit. on pp. 6–8).

[10] A. C. Melissinos, *Experiments in Modern Physics*, Academic Press, New York, 1966 (cit. on p. 7).

[11] G. F. Knoll, *Radiation Detection and Measurement*, 1st ed., John Wiley and Sons, 1979 (cit. on p. 8).

[12] H. Kolanoski and N. Wermes, *Teilchendetektoren – Grundlagen und Anwendungen*, 1st ed., Springer-Verlag, 2016 (cit. on pp. 8, 40).

[13] L. K. Schildgen et al., *teaching/labcourses/styx.git - Styx experiment software*, URL: https://gitweb.physik.uni-bonn.de/cgit/teaching/labcourses/styx.git/tree/STYXDoc/STYXInstruction/img/StyxBonn.jpg (cit. on p. 10).

[14] A. A. Affolder et al., *CDF central outer tracker*, Nucl. Instrum. Meth. **A526** (2004) 249 (cit. on p. 10).

[15] E. Zarkh, *Experimental Setup*, 2015, URL: https://www.brock.physik.uni-bonn.de/research/styx-experiment/experimental-setup (cit. on p. 11).

[16] E. Zarkh, *STYX Experiment: Further development*,
Master's Thesis: Physikalisches Institut, Universität Bonn, 2015 (cit. on pp. 11, 34).

[17] L. K. Schildgen et al., *teaching/labcourses/styx.git - Styx experiment software*,
URL: https://gitweb.physik.uni-bonn.de/cgit/teaching/labcourses/styx.git/
(cit. on p. 11).

[18] E. Thébault et al., *International Geomagnetic Reference Field: the 12th generation*,
Earth, Planets and Space **67** (2015) 79, ISSN: 1880-5981,
URL: https://doi.org/10.1186/s40623-015-0228-9 (cit. on p. 14).

[19] L. K. Schildgen et al., *teaching/labcourses/styx.git - Styx experiment software*,
URL: https://gitweb.physik.uni-bonn.de/cgit/teaching/labcourses/styx.git/tree/STYXDoc/STYXInstruction
(cit. on p. 15).

[20] M. Hohenwarter et al., *GeoGebra*, 2018, URL: https://www.geogebra.org/ (cit. on p. 18).

[21] C. B. Lang and N. Pucker, *Mathematische Methoden in der Physik*, 2nd ed.,
Springer-Verlag Berlin Heidelberg, 2005 (cit. on p. 36).

[22] A. Bartels and M. Stöckler, eds., *Wissenschaftstheorie, Ein Studienbuch*, 2nd ed.,
Mentis-Verlag, 2007 (cit. on p. 38).

[23] H. Schindler, *Garfield++ – simulation of tracking detectors*, 2018,
URL: http://garfieldpp.web.cern.ch/garfieldpp/ (cit. on p. 39).

[24] M. Weißenberg, *Neue Spurrekonstruktion für STYX mittels Hough-Transformation*,
Bachelor's Thesis: Physikalisches Institut, Universität Bonn, 2016 (cit. on p. 48).

APPENDIX A

Fit Results for the Drift-Time-Space Relation

The fit results for the *t*-*r* relation and the *r*-*t* relation that have been found as part of this thesis might be of interest for future improvements of the STYX event reconstruction and the STYX Monte Carlo software, respectively.

The fit results for fits of a cubic polynomial as given in Equation 5.1 are given in Table 5.1 for data and in Table 6.2 for a Monte Carlo simulation. The results may be implemented and tested in the STYX Monte Carlo software.

Both from data and from Monte Carlo simulation, the inverse polynomial

$$r(t) = q_0 + q_1 \times t + q_2 \times t^2 + q_3 \times t^3 \tag{A.1}$$

can be fitted to determine the *t*-*r* relation. The results extracted from data are contained in Table A.1, the ones from the Monte Carlo simulation in Table A.2. Implementing the results in the STYX event reconstruction software may lead to accurate results for the drift radius from a given drift time when the respective gas mixtures and voltages are used. This may help to improve the track reconstruction.

For a quick comparison, all tables also contain a line named “STYX code” containing the parameters that are used in STYX so far.

Table A.1: Resulting fit parameters of the *t*-*r* relation (Equation A.1) for different Ar:CO_2 mixtures and voltages determined from a data. The indices of the coefficients correspond to the power of the term in radius *r*. "STYX code" refers to the polynomial implemented in the reconstruction software of STYX.

Ar:CO_2	U/V	$q_0/10^{-3}$ mm	$q_1/(10^{-3}$ mm/ns)	$q_2/(10^{-6}$ mm/ns^2)	$q_3/(10^{-9}$ mm/ns^3)
82:18	1 800	1 221.1 ± 8.8	−19.0 ± 1.2	1 299 ± 46	−11 520 ± 480
82:18	1 810	1 109.3 ± 7.1	−18.29 ± 0.98	1 553 ± 37	−14 620 ± 390
82:18	1 820	1 082.1 ± 7.0	−15.92 ± 0.97	1 490 ± 36	−13880 ± 380
82:18	1 830	1 111.7 ± 4.5	−21.23 ± 0.63	1 683 ± 24	−15750 ± 250
82:18	1 840	1 080.3 ± 6.5	−20.22 ± 0.91	1 718 ± 34	−16070 ± 360
82:18	1 850	1 080.6 ± 8.6	−24.1 ± 1.2	1 958 ± 39	−18930 ± 470
86:14	1 800	1 040.2 ± 4.5	−20.16 ± 0.62	1 746 ± 23	−16080 ± 250
86:14	1 810	1 009.3 ± 7.6	−16.7 ± 1.1	1 775 ± 40	−17170 ± 420
86:14	1 820	1 025.7 ± 5.8	−18.56 ± 0.81	1 754 ± 30	−16550 ± 320
86:14	1 830	997.7 ± 7.8	−15.0 ± 1.1	1 721 ± 41	−16760 ± 430
86:14	1 840	992.1 ± 8.4	−12.6 ± 1.2	1 696 ± 44	−16910 ± 460
86:14	1 850	978.2 ± 8.7	−12.9 ± 1.2	1 740 ± 45	−17450 ± 480
90:10	1 800	1.007.8 ± 9.1	−11.1 ± 1.3	1 416 ± 48	−13240 ± 500
90:10	1 810	976.1 ± 7.6	− 4.5 ± 1.1	1 253 ± 39	−12140 ± 420
90:10	1 820	1 012.2 ± 8.8	− 2.4 ± 1.2	1 139 ± 46	−11260 ± 480
90:10	1 830	1 035.1 ± 7.2	− 0.57 ± 1.00	1 063 ± 37	−10660 ± 390
90:10	1 840	1 101.0 ± 8.1	− 4.4 ± 1.1	1 108 ± 42	−11060 ± 440
90:10	1 850	1 197.6 ± 8.8	5.1 ± 1.2	560 ± 46	− 6 020 ± 480
STYX code		11.4286	23.2707	1095.97	−9528.28

Table A.2: Resulting fit parameters of the *t*-*r* relation (Equation A.1) for different Ar:CO_2 mixtures and voltages determined from a Monte Carlo simulation. The indices of the coefficients correspond to the power of the term in radius *r*. "STYX code" refers to the polynomial implemented in the reconstruction software of STYX.

Ar:CO_2	U/V	$q_0/10^{-3}$ mm	$q_1/(10^{-3}$ mm/ns)	$q_2/(10^{-6}$ mm/ns^2)	$q_3/(10^{-9}$ mm/ns^3)
82:18	1 800	80 ± 10	69.9 ± 1.5	−0.262 ± 0.060	0.00151 ± 0.00064
82:18	1 810	81 ± 11	69.4 ± 1.6	−0.245 ± 0.063	0.00136 ± 0.00068
82:18	1 820	81 ± 10	69.7 ± 1.6	−0.253 ± 0.061	0.00139 ± 0.00065
82:18	1 830	80 ± 10	70.1 ± 1.5	−0.270 ± 0.060	0.00164 ± 0.00064
82:18	1 840	81 ± 10	69.9 ± 1.6	−0.258 ± 0.061	0.00146 ± 0.00066
82:18	1 850	82 ± 11	69.7 ± 1.6	−0.254 ± 0.064	0.00148 ± 0.00069
86:14	1 800	79.8 ± 9.7	64.7 ± 1.4	−0.284 ± 0.050	0.00234 ± 0.00051
86:14	1 810	81 ± 10	64.5 ± 1.5	−0.282 ± 0.054	0.00234 ± 0.00055
86:14	1 820	78.9 ± 9.3	64.9 ± 1.3	−0.294 ± 0.049	0.00246 ± 0.00049
86:14	1 830	78.5 ± 9.0	65.4 ± 1.3	−0.316 ± 0.047	0.00269 ± 0.00048
86:14	1 840	79.5 ± 9.4	65.1 ± 1.3	−0.298 ± 0.049	0.00246 ± 0.00050
86:14	1 850	80.1 ± 9.3	65.2 ± 1.3	−0.305 ± 0.049	0.00255 ± 0.00049
90:10	1 800	84 ± 10	57.0 ± 1.3	−0.239 ± 0.042	0.00183 ± 0.00038
90:10	1 810	85 ± 11	57.0 ± 1.3	−0.234 ± 0.043	0.00175 ± 0.00038
90:10	1 820	86 ± 11	57.1 ± 1.4	−0.243 ± 0.045	0.00187 ± 0.00040
90:10	1 830	88 ± 11	56.5 ± 1.4	−0.220 ± 0.046	0.00165 ± 0.00040
90:10	1 840	86 ± 11	57.4 ± 1.3	−0.255 ± 0.044	0.00199 ± 0.00039
90:10	1 850	88 ± 11	57.1 ± 1.4	−0.239 ± 0.045	0.00182 ± 0.00041
STYX code		11.4286	23.2707	1095.97	−9528.28

List of Figures

2.1 Primary cosmic ray energy spectrum . . . 5
2.2 Flux of secondary cosmic rays . . . 6
2.3 Operation Modes of Gaseous Detectors . . . 7

3.1 Image of the STYX detector . . . 10
3.2 Single straw drift time spectra . . . 12
3.3 Drift time spectra of malfunctioning straws . . . 13
3.4 Example Straw Mask . . . 14
3.5 Example Straw Mask . . . 16
3.6 Example Straw Mask . . . 16

4.1 Visualisation of Residuals . . . 18
4.2 Poorly and better fitted residuals . . . 19
4.3 Line fit to mean of residuals . . . 21
4.4 Number of Hits in the Straws of the Middle Module . . . 22

5.1 Straw stati for an Ar:CO_2 mixture of 90:10 . . . 27
5.2 Number of working straws for all mixtures . . . 27
5.3 Straw masks for an Ar:CO_2 mixture of 86:14 . . . 28
5.4 Straw stati for Ar:CO_2 mixture of 82:18 . . . 28
5.5 Drift time spectra for different gas mixtures . . . 30
5.6 Drift time spectra before and after calibration for two gas mixtures . . . 31
5.7 Histogram for *r-t* relation . . . 31
5.8 Histogram for the *r-t* relation extracted from data . . . 32
5.9 Histogram for the *t-r* relation extracted from data . . . 34
5.10 Straw efficiency: expected and observed hits . . . 35
5.11 Efficiencies for different gas mixtures . . . 37

6.1 Example for one simulation point . . . 41
6.2 Polynomials for *r-t* relation of the standard gas mixture . . . 42
6.3 Polynomials for *t-r* relation of the standard gas mixture . . . 42
6.4 Polynomials for *t-r* relation . . . 42

7.1 Number of hits per Event . . . 44
7.2 Straw mask from 50 000 events . . . 44
7.3 Straw mask from 300 000 events . . . 44
7.4 Number of Events for Calibration . . . 45

List of Tables

4.1 Widths of residuals 20
4.2 Mean values of residuals 20

5.1 Fit parameters for space-drift-time relation from data 33
5.2 Efficiency for different gas mixtures 36

6.1 Parameters given to the simulation programme Garfield++ 40
6.2 Fit parameters for space-drift-time relation from simulation 40

A.1 Fit parameters for *t*-*r* relation from data 52
A.2 Fit parameters for *t*-*r* relation from simulation 52